VYSOKÉ UČENÍ TECHNICKÉ V BRNĚ

Fakulta strojního inženýrství

DIPLOMOVÁ PRÁCE

Brno, 2017 Bc. Ivo Hlavička

VYSOKÉ UČENÍ TECHNICKÉ V BRNĚ
BRNO UNIVERSITY OF TECHNOLOGY

FAKULTA STROJNÍHO INŽENÝRSTVÍ
FACULTY OF MECHANICAL ENGINEERING

ÚSTAV FYZIKÁLNÍHO INŽENÝRSTVÍ
INSTITUTE OF PHYSICAL ENGINEERING

CYKLOTRONOVÁ REZONANCE DIRACOVÝCH ELEKTRONŮ V SELENIDU BISMUTITÉM
CYCLOTRON RESONANCE OF DIRAC ELECTRONS IN BISMUTH SELENIDE

DIPLOMOVÁ PRÁCE
MASTER'S THESIS

AUTOR PRÁCE — **Bc. Ivo Hlavička**
AUTHOR

VEDOUCÍ PRÁCE — **Ing. Miroslav Bartošík, Ph.D.**
SUPERVISOR

BRNO 2017

VYSOKÉ UČENÍ TECHNICKÉ V BRNĚ
FAKULTA STROJNÍHO INŽENÝRSTVÍ

Zadání diplomové práce

Ústav:	Ústav fyzikálního inženýrství
Student:	**Bc. Ivo Hlavička**
Studijní program:	Aplikované vědy v inženýrství
Studijní obor:	Fyzikální inženýrství a nanotechnologie
Vedoucí práce:	**Ing. Miroslav Bartošík, Ph.D.**
Akademický rok:	2016/17

Ředitel ústavu Vám v souladu se zákonem č.111/1998 o vysokých školách a se Studijním a zkušebním řádem VUT v Brně určuje následující téma diplomové práce:

Cyklotronová rezonance Diracových elektronů v selenidu bismutitém

Stručná charakteristika problematiky úkolu:

Selenid bismutitý (Bi2Se3) se řadí do skupiny takzvaných topologických izolátorů, tj. materiálů s charakteristickou inverzní pásovou strukturou a spin–polarizovanými povrchovými stavy s lineární disperzí. Tyto netypické vlastnosti tohoto materiálu lze využít při vývoji nových metod například v oblasti spintroniky či ve výrobě magnetoeletrických zařízení.
Cílem této práce bude charakterizovat povrchové stavy z hlediska elektronové disperze (měření efektivní cyklotronové hmotnosti) a též z hlediska rozptylových mechanismů (měření elektronové mobility), to vše za použití magneto–optických měření a měření transportu elektrického náboje.

Cíle diplomové práce:

1) Vypracovat rešerši, jež shrnuje poznatky na téma topologických izolátorů.
2) Provést měření za pomocí infračervené spektroskopie v nízkých a vysokých magnetických polích.
3) Provést transportní měření použitím dvoubodové resp. čtyřbodové metody.
4) Analyzovat a interpretovat získané výsledky.

Seznam doporučené literatury:

Qi X. and Zhang S. The quantum spin Hall effect and topological insulators. In: Physics Today 63.1 (2010), p. 33. issn: 00319228. doi: 10.1063/1.3293411. arXiv: 1001.1602.

Hasan M. Z. and Kane C. L. Colloquium: Topological insulators. In: Reviews of Modern Physics 82.4 (2010), pp. 3045–3067. issn: 00346861. doi 10.1103/RevModPhys.82.3045. arXiv: 1002.3895.

Orlita M. et al. Classical to quantum crossover of the cyclotron resonance in graphene: A study of the strength of intraband absorption. In: New Journal of Physics 14 (2012). issn: 13672630. doi: 10.1088/1367-2630/14/9/095008. arXiv: 1205.1118.

Orlita M. and Potemski M. Dirac electronic states in graphene systems: Optical spectroscopy studies. Semiconductor Science and Technology (2010), 25(6), 63001.

Termín odevzdání diplomové práce je stanoven časovým plánem akademického roku 2016/17

V Brně, dne

L. S.

prof. RNDr. Tomáš Šikola, CSc. ředitel ústavu	doc. Ing. Jaroslav Katolický, Ph.D. děkan fakulty

ABSTRACT

Bi_2Se_3 belongs to a class of topological insulators—materials characterized by a intriguing electronic band structure, with a characteristic conical band on the surface. In this master thesis, the optical response of this material is explored in the infrared spectral range and in a broad range of magnetic fields. We mainly focus on the absorption of light due to free charge carriers having, when the magnetic field is applied, a form of cyclotron resonance. We find that the experimentally observed response is consistent with expectations for massive electrons in bulk rather than massless particles on the surface.

KEYWORDS

bismuth selenide, Fourier transform infrared spectroscopy, topological insulator, cyclotron resonance

ABSTRAKT

Bi_2Se_3 se řadí do skupiny topologických izolátorů—materiálů charakteristických svou pozoruhodnou pásovou strukturou, vyznačující se přítomností Diracovských povrchových stavů s lineární disperzí. V této práci se zabýváme optickou odezvou tohoto materiálu v infračerveném spektru za přítomnosti magnetických polí. V takovém případě probíhá absorpce, jež má charakter cyklotronové rezonance, na volných nosičích náboje. Výsledky experimentů ukazují, že pozorovaná odezva odpovídá spíše modelu hmotných elektronů ve vnitřních stavech nežli modelu nehmotných elektronů na povrchu.

KLÍČOVÁ SLOVA

selenid bismutitý, Fourierovská infračervená spektroskopie, topologický izolátor, cyklotronová rezonance

HLAVIČKA, Ivo *Cyclotron resonance of Dirac electrons in bismuth selenide*: master's thesis. Brno: Brno University of Technology, Faculty of Mechanical Engineering, Ústav fyzikálního inženýrství, 2017. 50 p. Supervised by Ing. Miroslav Bartošík, Ph.D.

DECLARATION

I declare that I have elaborated my master's thesis on the theme of "Cyclotron resonance of Dirac electrons in bismuth selenide" independently, under the supervision of the master's thesis supervisor and with the use of technical literature and other sources of information which are all quoted in the thesis and detailed in the list of literature at the end of the thesis.

As the author of the master's thesis I furthermore declare that, concerning the creation of this master's thesis, master's thesis, I have not infringed any copyright. In particular, I have not unlawfully encroached on anyone's personal copyright and I am fully aware of the consequences in the case of breaking Regulation § 11 and the following of the Copyright Act No 121/2000 Vol., including the possible consequences of criminal law resulted from Regulation § 152 of Criminal Act No 140/1961 Vol.

Brno ....

(author's signature)

Acknowledgement

I would like thank my supervisor Milan Orlita for the time he spent answering quanta of my questions, leading and proofreading my thesis and teaching me to drink coffee. I am very thankful for meeting everyone from the Nanophysics group led by the great Marek Potemski at LNMCI Grenoble, namely Artur Slobodeniuk, who never hesitated to explain me every little physical concept, and Benjamin Piot, who helped me with magneto-transport measurements. I also want to thank my second supervisor Miroslav Bartošík for all the help and advice on my thesis.

Ivo Hlavička

CONTENTS

1 INTRODUCTION

In the last two decades, the condensed matter physics witnessed a surge of interest in the perspective area of the topological field theory. Concepts built on its basis, such as the quantum Hall effect, opened new areas in physics and through the years of research pushed the effort to a new unusual applications. One of them are the topological insulators—a novel class of materials with distinctive non-trivial electronic band structure, allowing them to host linearly dispersed electronic states on the surface, while at the same time being insulating in the bulk.

Among many different types of topological insulators, the very promising one is the bismuth selenide (Bi_2Se_3) with its robust energy band gap. One of the drawbacks, however, is its problematic intrinsic doping, resulting in high carrier concentration of the bulk states. This effect is suppressed by fabricating a novel Bi_2Se_3 heterostructure, proposing better crystal quality and higher mobility of the surface states. It is still, however, a subject of development and needs to be studied extensively.

To this end, magneto-optical spectroscopy serves as an experimental method capable of thorough electronic structure characterization, on par with angle-resolved photo-emission spectroscopy or magneto-transport measurements. As a material with characteristic Dirac-like dispersion of surface states, Bi_2Se_3 features specific cyclotron resonance spectra. Using infrared spectroscopy in magnetic fields, we are able to reveal the details of Landau level energy spectra and properly characterize the system.

To give a basic insight into the peculiarities of the topological insulators, we briefly introduce this field in Chapter 2, as well as introducing the Bi_2Se_3 heterostructure. In the Chapter 3, we describe a simple model on which the analysis of our magneto-optical analysis of Bi_2Se_3 will be based, both in quasi-classical regime and quantum regime. Chapter 4 deals with the experimental setup consisting of Fourier transform infrared spectrometer and magnet installation. Finally, the experimental data obtained from magneto-optical experiments are presented in Chapter 5.

The experimental work in this thesis was realized as a part of two ERASMUS+ Internships at *Laboratoire National de Champs Magnétiques Intenses* (LNCMI) in Grenoble, France.

2 TOPOLOGICAL INSULATORS

2.1 Introduction

The band structure theory, describing the electronic properties of crystals and other periodic systems, belongs to most crucial concepts of current condensed-matter physics. Following this theory, electrons in crystals are allowed to occupy only specific energy states organized into bands. Such an approach allows us to classify the systems as insulators, semi-conductors or metals, depending on the position of their Fermi energy, which corresponds to the highest energy occupied by electrons with respect to forbidden states, called band gaps. So if the Fermi energy lies within an energy band, the system then behaves as a metal. On the other hand if the Fermi energy lies in the large energy band gap, no mobile states are available and the system becomes insulating. In between lies the area of semiconductors, where the energy band gap is sufficiently small to allow transitions to higher states [1].

This model has been very successful for decades and became the vital element in the physics as many electrical, optical, and even some magnetics properties of crystals can be explained in terms of the corresponding band structure. However, all great achievements of band structure theory considered, it became rather insufficient to describe for example inhomogeneous electronic systems or, more importantly, the novel two-dimensional electronic phases [2].

When in 1980 Klaus von Klitzing discovered the existence of the quantum Hall effect (QHE), which occurs when electrons confined to two dimensions are placed in a strong magnetic field [3], the old paradigm of employing the band structure failed as it was not able to define such state adequately. From the band structure point of view, this system should be an insulator, as the Fermi energy lies in the gap between Landau levels. However, conducting edge states were still found to occur in such 2D systems. This was the first example of a quantum state which is topologically distinct from all states of matter known before.

Topology is a branch of mathematics that studies the properties of objects invariant under smooth deformations, a classic example being a doughnut transforming into a coffee cup or sphere transforming into ellipsoid. Generally, topological classification discards all small details and focuses on the fundamental distinction of shapes. The different topological classes can be distinguished by one or more indexes—so-called topological invariants. These numbers are discrete, and therefore cannot be changed continuously simply by a smooth deformation. One can smoothly transform sphere into the shape of red blood cell as their invariant is identical, but there is no continuous transformation from a sphere to a torus, hence the invariant is different [2].

Interestingly, this topological concept can be applied to electronic systems with a band gap, where the notion of smooth deformation can be defined. One can define such deformation as a change in the Hamiltonian which does not close the gap. Then, according to the general definition [4], one gapped state cannot be smoothly deformed to another gapped state in a different topological class, unless a quantum state transition occurs during which the system becomes *gapless*.

In case of the quantum Hall effect, the transition appears at the interface between 2D electron gas and vacuum. The former is characterized by a quantized energy gap in the bulk separating Landau levels, whereas the latter is insulating state with the energy gap corresponding to the creation of positron and electron. As they belong to the different topological classes, the gap at the interface disappears and 1D gapless surface states emerge instead. Each of these edge channels exhibits a conductance quantized as Ne^2/h that is characteristic for one-dimensional transport. These conducting edge states are moreover chiral—they propagate in a single direction, only depending of the edge orientation and the magnetic field orientation. Furthermore, these states are insensitive to disorder because there are no states available for backscattering [5].

The quantum Hall states belong to a topological class in which the so-called time-reversal symmetry (TR) is explicitly broken [4,6,7] by presence of an external magnetic field. In the last decade, a new topological class of materials has been theoretically predicted and experimentally observed—quantum spin Hall insulators—which, in contrast, are TR invariant and do not require an applied magnetic field [2,4,8,9]. In the following chapters we briefly elaborate on the development of these 2D topological insulators such as HgTe/CdTe quantum wells and after that we discuss the attributes of 3D topological insulators as a next evolutionary step, with special emphasis on bismuth selenide which was the studied in this work.

2.2 Two-dimensional topological insulators

The concept of quantum spin Hall (QSH) insulators or 2D topological insulators was first introduced in 2005 by Kane and Mele [10] and by Bernevig and Zhang [11] a year later when studying the effects of a spin-orbit coupling (SOC) in graphene. For the quantum Hall effect to appear, one needs to employ a strong magnetic field. In case of QSH however, the role of the magnetic field is played by this intrinsic spin-orbit field.

Graphene, being a hexagonal lattice of light carbon atoms [12], shows rather weak effects of SOC and it is therefore quite difficult to find an experimental evidence of the QSH [13]. Clearly, a better place to look for a demonstration of SOC would be

in materials made from heavy elements near the bottom part of the periodic table. To this end, Bernevig, Hughes and Zhang had the idea to consider quantum well structures of HgCdTe [11]. This prediction was soon crowned by success when König indeed observed in 2007 quantum spin Hall state in CdTe/HgTe/CdTe quantum wells [9].

For both HgTe and CdTe, the relevant bands near the Fermi level are close to the Γ point of the Brillouin zone ($k = 0$). These bands are s-type and p-type, where, in case of the CdTe, the band ordering is similar to GaAs—the s-type conductive band has higher energy at the Γ point than p-type valence band, i.e., they are separated by a large ($\sim$1.5 eV) band gap [8]. HgTe, on the other hand exhibits stronger SOC than CdTe due to presence of mercury atom which results in *reverse* order of bands (see Fig. 2.1). The negative energy gap of -300 meV between the bands indicates that the p-band, which usually forms the valence band, has higher energy at Γ point than s-band [11].

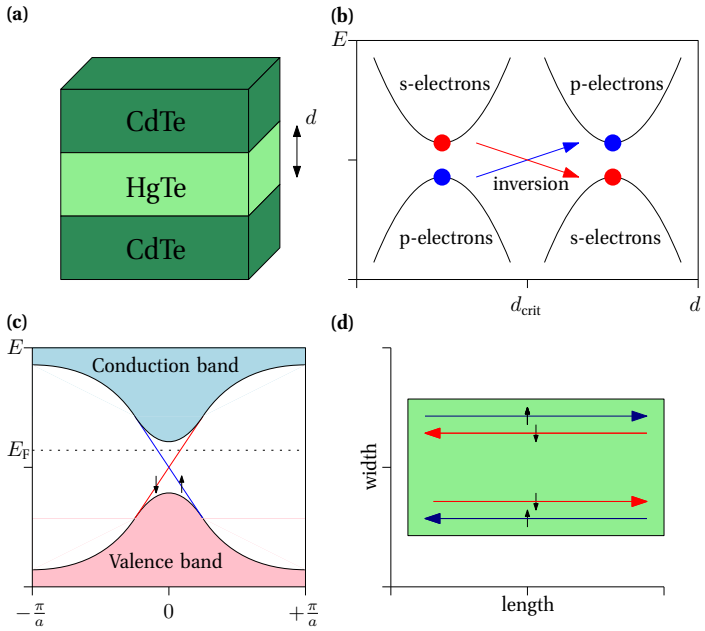

Fig. 2.1: Two-dimensional topological insulator in (a) HgCdTe quantum well. (b) A schematic depiction of 2D QW states crossing as a function of the well thickness. (c) Resulting edge state dispersion where the spin up and down electrons propagate in opposite directions. (d) Such spinful system has four 1D basic channels, which are spatially separated by QSH bar. The upper edge contains a forward mover with spin up and backward mover with spin down, and conversely for the lower edge. Adapted from [6].

Due to this band inversion, HgTe represents a different topological class than

CdTe and therefore the gap disappears at the interface between them in a similar way as in the case of the QHE. Moreover, growing the quantum well layer of HgTe with different thickness allows fine tuning of the electronic structure. If the thickness d_{QW} of quantum well (QW) falls below a critical value $d_{\mathrm{crit}} = 6.3$ nm, the bulk character of HgTe disappears and the structure retains the normal non-inverted CdTe-like properties [9]. By increasing the thickness, the bands in QW begin to invert and at critical d_{crit} the bands cross. This way, one can carefully study the transition from a trivial insulator to a topological insulator.

Although bearing a resemblance to QHE, the edge states of QSH insulator are different in one fundamental aspect—the pair of linearly dispersed edge states of a QSH insulator propagate in both directions, depending on their *spin*. Contrary to the QHE, the QSH edge states exhibit so-called *helicity*, i.e., the states with opposite spin counterpropagate at a given edge as seen in Fig. 2.1d. Thanks to the 1D character of the spin-polarized edge states, they are also protected against backscattering, particularly against backscattering on non-magnetic impurities [14].

Besides HgCdTe quantum wells, multiple other 2D materials and structures were predicted and/or experimentally observed to exhibit QHS phase. For example bilayers of bismuth [15], or inverted InAs/GaSb semiconductor quantum wells [16], or GaAs, where the role of SOC is played by the shear strain gradients imposed on the crystal lattice [17].

2.3 Three-dimensional topological insulators

The next logical step, after the discovery of 2D topological insulators, was to ask if this concept could be generalized to three dimensions. The "theoretical" answer was given in 2007 when three theoretical groups lead by Kane, Moore and Roy theorized the existence of 3D topological phase in $Bi_{1-x}Sb_x$, strained α-Sn, strained HgTe, $Pb_{1-x}Sn_xTe$, and β-HgS compounds [18–20].

Similar to the their 2D counterparts, the band inversion transition at the Γ point is also driven by spin-orbit coupling and there is also insulating gap in the bulk. The dispersion relation of gapless edge states or surface states in this case now resembles so-called Dirac cone, which also appears, for example, at the corners of the hexagonal Brillouin zone of the graphene [12, 13]. In case of graphene, however, the electronic states form 2 Dirac cones (4 cones if we take into account spin of the electrons), but there is only single Dirac cone in case of 3D topological insulators and it is not spin degenerate [19].

First 3D topological insulator was experimentally discovered in 2008 at Princeton Univeristy by Zahid Hasan and coworkers in semiconducting alloy $Bi_{1-x}Sb_x$ [21],

where the unusual band structure was mapped using angle-resolved photoemission spectroscopy (ARPES). Pure bismuth is a semimetal with a strong SOC and electronic band structure comprised the overlapping conduction and valence band as visible on Fig. 2.2. The L_s and L_a bands disperse nearly linearly and can be described in same manner as Dirac electrons with small or even zero mass. Increasing the amount of antimony in the alloy slowly shifts band at T point to lower energies and also closes the gap between L_s and L_a. At $x \approx 0.04$, the gap is fully closed and the true 3D massless point emerges. Higher values result in a reopening of the energy band gap, but this time with the L_s and L_a bands *inverted*. For $x > 0.07$ the top valence band at T point drops below L_s and the alloy becomes an insulator. ARPES spectra were obtained by Hasan *et al.* for alloy $Bi_{0.91}Sb_{0.09}$, where the system is direct-gap insulator with inverted massive Dirac bulk bands. In this gap, several surface states were observed (Fig. 2.2) and using spin-resolved ARPES it was determined that these states are non-degenerate and indeed spin-polarized.

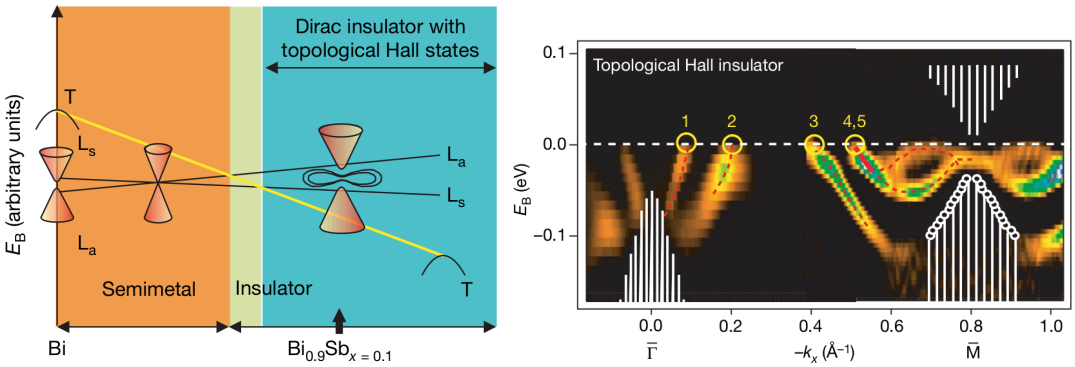

Fig. 2.2: Topological gapless states in $Bi_{1-x}Sb_x$. Left: schematic variation of bulk band energies as a function of antimony concentration x. Right: ARPES data on the (111) surface of $Bi_{0.9}Sb_{0.1}$ which probes the occupied surface states as a function of momentum on the line connecting Γ and M point in the surface Brillouin zone. Only the surface states cross the Fermi energy five times. This and several other ARPES measurements [21] establishes that $Bi_{1-x}Sb_x$ alloy is indeed topological insulator. Picture adapted from [21].

Nevertheless, the existence of topological phase in $Bi_{1-x}Sb_x$ is all but robust. Due to being an alloy with random substitutional disorder, its electronic structure is well defined only within specific conditions. Alloys also tend to have impurity bands inside the bulk energy band gap, which could overlap with the surface states. To avoid such problems, it is desirable to search for materials which are stoichiometric—the ratio of different atoms in all molecules reflects the general formula of the compound. These problems combined with bulk band gap of only 50 meV [4,21] sparked a search

for simpler and more thermally stable systems.

In 2009 two concurrent groups—team of Haijun Zhang from Chinese Academy of Sciences and team of YuQi Xia from Princeton University theoretically predicted robust topological insulators in Bi_2Se_3, Bi_2Te_3 and Sb_2Te_3 [5, 22]. Soon after, the ARPES spectra (see Fig. 2.3) confirmed existence of a single Dirac cone in the surface states band structure in all of them [22–24] This second generation of 3D topological insulators has in comparison to $Bi_{1-x}Sb_x$ much bigger band gap of ∼200 meV and one may therefore expect to observe topological properties even at room temperature.

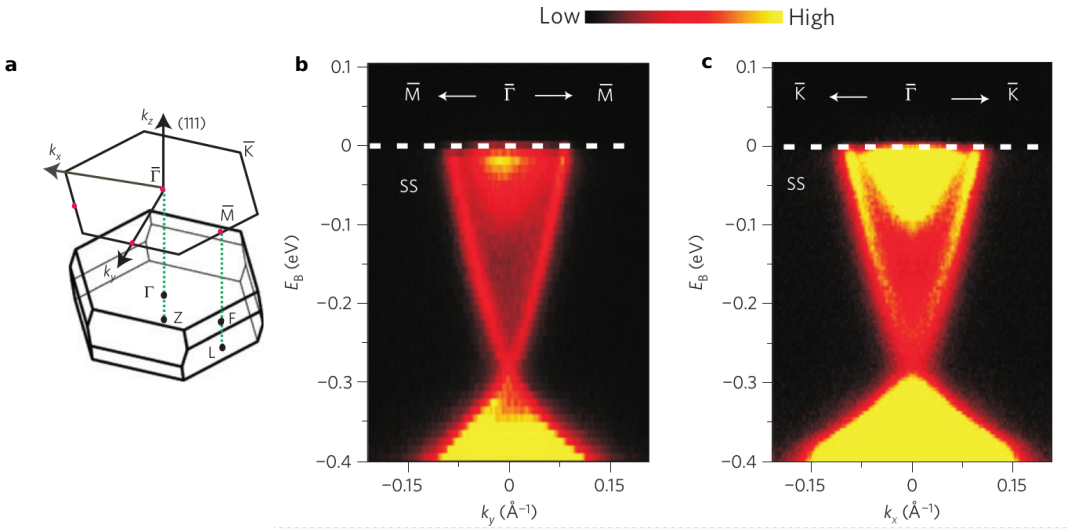

Fig. 2.3: (a) A schematic diagram of the bulk 3D Brillouin zone of Bi_2Se_3 and the 2D Brillouin zone of the projected (111) surface. ARPES spectra of surface electronic band dispersion on Bi_2Se_3 near Γ point along the (b) Γ–M and (c) Γ–K momentum-space cuts. Picture adapted from [22].

Another advantage of the Bi-Se-Te family is the fact, that these are compounds with rather high crystal quality and due to the layered nature it is possible to exfoliate thin sheets down to single layers. Moreover, nanostructures can be prepared using methods like molecular beam epitaxy. Owing to these specific qualities, Bi-Se-Te family soon emerged as an attractive candidate for the study of topological surface states.

In our case, we focused our research on infrared spectroscopy of bismuth selenide (Bi_2Se_3) and thus this compound will be subject of the following chapter.

2.4 Bismuth selenide

Bismuth selenide is certainly not a material that emerged only recently—it has been long studied for its thermoelectric properties and used for example in thermoelectric refrigeration [25, 26]. Due to its technological importance and the wealth of experimental data, the picture of crystal lattice of Bi_2Se_3 is very well established.

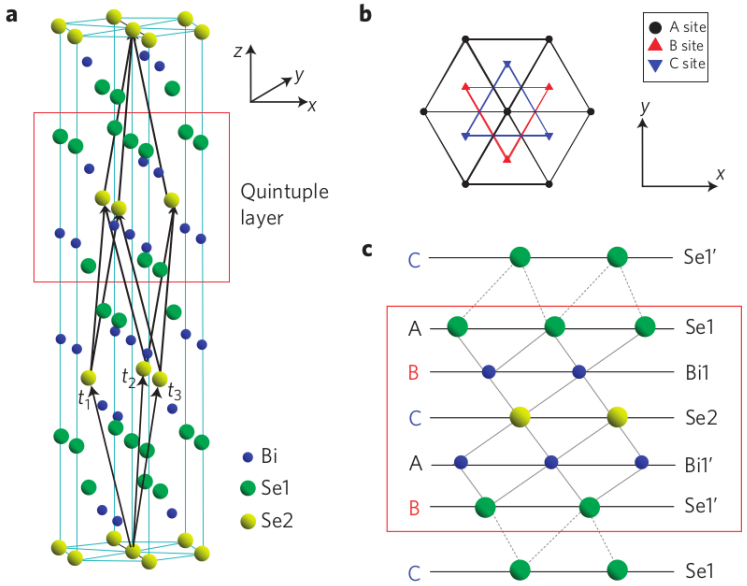

Fig. 2.4: (a) Crystal structure of bismuth selenide with three primitive lattice vectors denoted $t_{1,2,3}$. A quintuple layer with Se1-Bi1-Se2-Bi1'-Se1' is indicated in the red square. (b) Top views along the z-direction. The triangle lattice in one quintuple layer has three different positions, denoted as A, B and C. (c) Side view of the quintuple layer structure. Image taken from [5].

As well as the rest of the Bi-Se-Te family, Bi_2Se_3 shares the same rhombohedral crystal structure consisting of five atoms in one unit cell. As we can see from the Fig. 2.4, Bi_2Se_3 has layered structure with a triangle lattice within one five-atom layer. It has a trigonal axis (three-fold rotation symmetry), defined as the z axis, a binary axis (two-fold rotation symmetry), defined as the x axis, and a bisectrix axis (in the reflection plane), defined as the y axis. The material consists of five-atom layers arranged along the z-direction, known as quintuple layers (QL). Each quintuple layer consists of five atoms with two equivalent Se atoms (denoted as Se1 and Se1' in Fig. 2.4c), two equivalent Bi atoms (denoted as Bi1 and Bi1' in Fig. 2.4c) and a third Se atom (denoted as Se2 in Fig. 2.4c). The coupling is strong between two atomic layers within one quintuple layer but much weaker, predominantly of the van der Waals type, between two quintuple layers [5].

While the Bi_2Se_3 was proposed to be a nearly ideal example of a 3D topological insulator thanks to its material qualities, as discussed in previous chapter, it also could not avoid certain drawbacks, major one being the strong intrinsic n-type doping [8, 27–29]. Such doping occurs due to naturally present Se vacancies that act as electrical donors [30]. This results in the shift of the Fermi energy to higher values and instead of conductance coming purely from surface states, the parasitic bulk conductance dominates.

To effectively tune the Fermi energy close to the Dirac point of the surface states, one can employ controllable extrinsic doping. Several experiments with variety of doped elements were performed, for example copper [28, 31, 32], calcium [29, 33], antimony [30], that showed positive results. Nevertheless, such doping indeed suppreses the bulk cunductivity, however, it also strongly reduces the electronic quality of the material [30,34]. Considering that both high mobilities and low carrier densities are essential to revealing quantum nature of any materials, a solution to this problem lies rather elsewhere.

Another approach would be increasing the surface to volume ratio of the material i.e. manufacturing thin films [35–37] using exfoliation or molecular beam epitaxy. Although, such small dimensions cause another problem—the conducting channel provides an intersurface conduction path, and this causes the top and bottom topological surface states to be coupled into a one single channel [28]. One has to take into account also the pronounced surface defects which are also source of carriers.

It is natural to postulate that a chemically and structurally matched substrate should simultaneously suppress both interfacial and bulk defects, which are responsible for low mobilities and high carrier densities in TI films. At the moment, such a single-crystal substrate does not exist with the current selections either increasing bulk defects or creating interfacial defects [27,35–37].

2.4.1 Bismuth selenide heterostructure

One of the proposed solutions to aforementioned issues is the heterostructure grown using the molecular beam epitaxy (MBE) and consisting of Bi_2Se_3, In_2Se_3 and $(Bi_{0.5}In_{0.5})Se_3$ designed and fabricated by the team of Seongshik Oh from the State University of New Jersey [27].

All these three compounds share the same layered structure with covalently bonded QLs, which are held together by the weak van der Waal's (vdW) force [38,39]. Because of vdW bonding, Bi_2Se_3 can be grown on substrates with large lattice mismatch because the film relaxes to its bulk lattice constant within the first QL. This allows the defects formed at the interface to be isolated within the first layer

and subsequent layers have substantially suppressed defects even when grown on conventional substrates with large lattice mismatch such as $Al_2O_3(0001)$ [40].

Additionally, when Bi_2Se_3 is grown on top of a substrate with a better lattice match, such as Si(111) and InP(111), the interfacial defects are suppressed, but transport measurements show that additional bulk defects are created, which are likely due to the more reactive substrate surface [37]. In_2Se_3 and $(Bi_{0.5}In_{0.5})Se_3$ with their layered structure minimize strong chemical bonding at the interface and with the small lattice mismatch to Bi_2Se_3, serve as an ideal candidate to create a buffer layer for Bi_2Se_3.

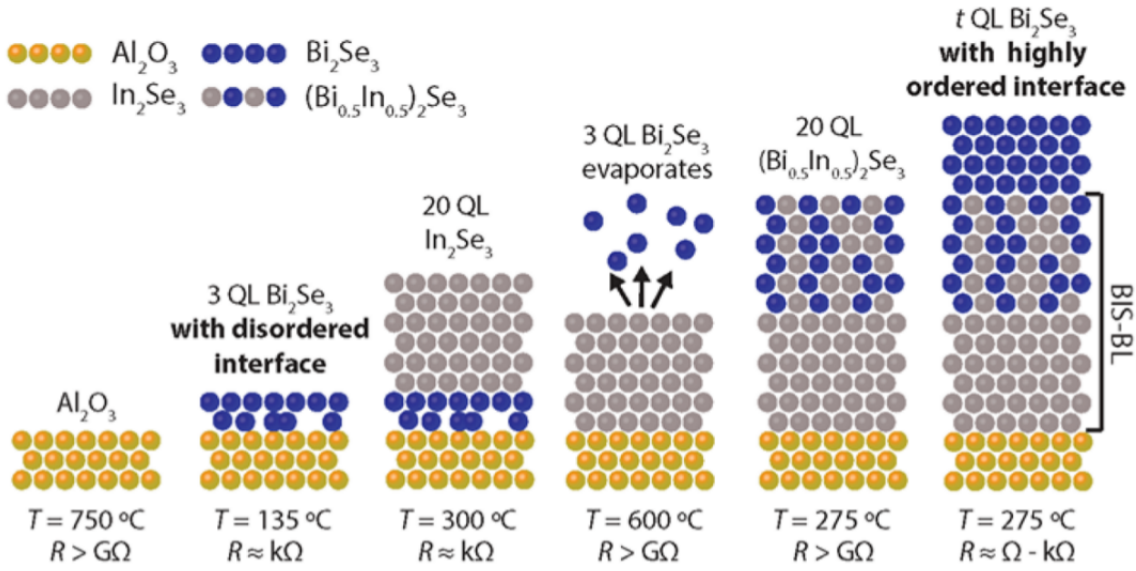

Fig. 2.5: Growth process of Bi_2Se_3 films on the 20 QL In_2Se_3 and 20 QL $(Bi_{0.5}In_{0.5})Se_3$ buffer layer. Corresponding growth temperature T and sheet resistance R are shown as well. Picture adapted from [27].

The fabrication method of such a heterostructure is schematically depicted in Fig. 2.5. Unlike Bi_2Se_3, In_2Se_3 has at least three phases [41], and when deposited directly onto the poorly lattice matched Al_2O_3 substrate it grows in a disordered form. Therefore, to grow a high-quality single-phase In_2Se_3 layer requires an initial seed layer of 3 QL Bi_2Se_3 that is deposited at 135 °C; this serves as a template for the 20 QL thick In_2Se_3 layer to be deposited at 300 °C. At this stage, the underlying 3 QL of Bi_2Se_3 remains conducting, which is undesirable as it creates extra conduction channel. In order to make it electrically insulating, this entire layer is heated up to 600 °C where the Bi_2Se_3 seed layer diffuses through the In_2Se_3 and evaporates away, which leaves behind the high quality, insulating In_2Se_3 layer directly on the Al_2O_3 substrate. On top of this, a 20 QL thick insulating layer of $(Bi_{0.5}In_{0.5})Se_3$ is then deposited at 275 °C, which acts to suppress In diffusion into the Bi_2Se_3 layer [39].

This entire structure forms the BIS-BL—a high quality virtual-substrate for Bi_2Se_3 to be deposited at 275 °C.

Transport measurements are the most sensitive probe to study the presence of defects that supply carriers and cause defect induced scattering. Therefore, a comparison of the defect density in Bi_2Se_3 grown on the BIS-BL to films grown on Al_2O_3(0001) and Si(111) substrates, is made in Fig. 2.6ab where the sheet carrier density and mobility were extracted from the low magnetic field Hall measurement as a function of thickness. As shown in Fig. 2.6b, the highest mobility for Bi_2Se_3 grown on BIS-BL is about an order of magnitude larger than the mobility of films grown on Al_2O_3(0001) and Si(111), and this directly shows that BIS-BL significantly suppresses the net defect density [27].

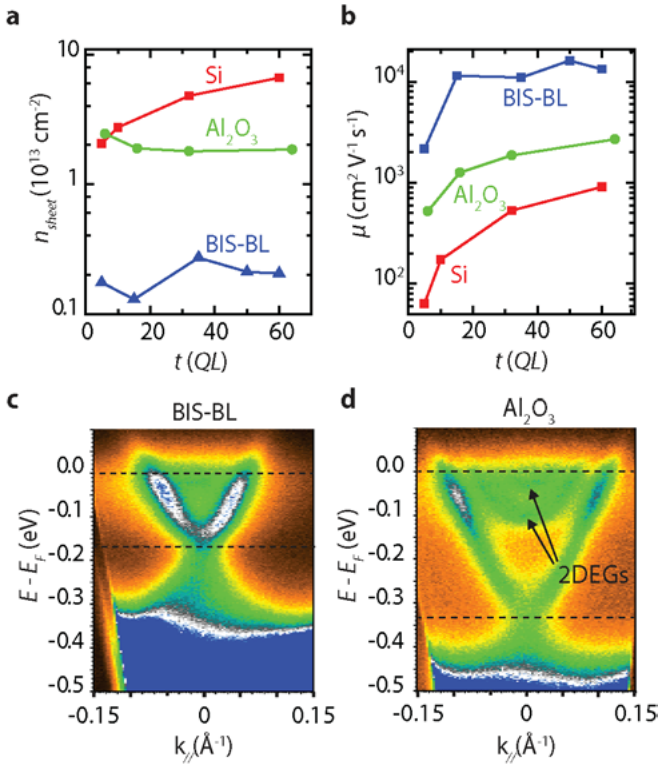

Fig. 2.6: Comparison of (a) sheet carrier densities and (b) Hall mobilities of Bi_2Se_3 films grown on BIS-BL, Al_2O_3(0001) and Si(111) for various film thicknesses. ARPES of Bi_2Se_3 grown on (c) BIS-BL and (d) Al_2O_3(0001). Picture taken from [27].

Furthermore, Fig. 2.6cd also shows the ARPES spectra of a 30 QL thick Bi_2Se_3 films grown on BIS-BL (Fig. 2.6c) and a 50 QL thick Bi_2Se_3 grown on Al_2O_3 (Fig. 2.6d), both clearly showing the topological surface states bands, which confirms their non-trivial topology. Further, we can compare the position of the surface Fermi energy (E_F) of Bi_2Se_3 grown on both substrates. For the film grown on Al_2O_3,

E_F lies ∼0.33 eV above the Dirac point. At this level, the conduction band is clearly occupied by two-dimensional electron gas (2DEG) states that form due to downward band bending of bulk conduction band near the surface. In contrast, for the film grown on BIS-BL E_F is only ∼0.17 eV above the Dirac point, which implies that on the surface only the topological surface states bands are occupied. The lower E_F observed in films grown on BIS-BL compared to films grown directly on Al_2O_3 is consistent with the lower carrier density observed in transport measurements [27].

For the purposes of magneto-transmission spectra measurements, which are the main objective of this thesis, the team of Seongshik Oh fabricated total of 4 samples with 6 QL, 8 QL, 10 QL, and 16 QL, respectively, thick Bi_2Se_3 films. As the top layer of the Bi_2Se_3 is sensitive to ambient contamination, the final step consisted of adding a ∼50 nm of MoO_3 as a protection in between the experiments. These samples were characterized by low-field cyclotron resonance and Faraday rotation measurements in the group of Peter Armitage at John Hopkins University and then delivered to LNCMI for further optical studies at high magnetic fields.

The subject of following chapter will be the simple model describing optical response in magnetic field for such type of topological insulator.

3 MAGNETO-OPTICAL RESPONSE IN CONVENTIONAL AND DIRAC-TYPE SYSTEMS

Infrared spectroscopy in magnetic field is very convenient experimental method providing insight into electronic band structure in the framework of effective mass and the related resonant absorption of light at the cyclotron frequency. Through the years it became widely applied method, usually complementary to transport experiments, for probing all sorts of electronic systems including graphene [42–44] which features the characteristic Dirac behaviour of carriers.

As a material with linear Dirac-like dispersion of surface states, Bi_2Se_3 exposed to high magnetic fields shall exhibit well defined transitions between Landau quantized energy levels similarly as in the case of the graphene—yielding the linear in $\sqrt{B}$ response [45]. The following sections are devoted to the derivation and description of a simple model of Landau quantized system and its magneto-optical response for both free electron gas with parabolic dispersion and for free electrons in Dirac system.

3.1 Landau quantization in conventional systems

Despite our interest in surface Dirac electrons in Bi_2Se_3, let us first derive the basic spectrum of Landau levels (LL) of conventional non-Dirac 2D electron gas in a magnetic field as it will be crucial for magneto-transmission spectra analysis presented later on.

We assume the magnetic field $\vec{B} = (0, 0, B)$ in z-direction and use the Landau gauge $\vec{A} = (0, Bx, 0)$. Applying Peierls substitution $\vec{p} \to \vec{p} = (\vec{p} - e\vec{A})$, the free electron Hamiltonian reads:

$$\hat{H} = \frac{\vec{p}^2}{2m} \qquad \longrightarrow \qquad \hat{H} = \frac{(\vec{p} - e\vec{A})^2}{2m}. \tag{3.1}$$

The Schrödinger equation $\hat{H}\psi(\vec{r}) = E\psi(\vec{r})$ now becomes

$$\frac{1}{2m}\left[\left(-i\hbar\frac{\partial}{\partial x}\right)^2 + \left(-i\hbar\frac{\partial}{\partial y} - eBx\right)^2\right]\psi(\vec{r}) = E\psi(\vec{r}). \tag{3.2}$$

As one of the terms of $\vec{A}$ depends on x, we assume the ansatz in the form of

$$\psi(\vec{r}) = \varphi(x)e^{ik_y y}. \tag{3.3}$$

Substituting this in (3.2) yields

$$\left[-\frac{\hbar^2}{2m}\left(\frac{\mathrm{d}^2}{\mathrm{d}x^2}\right)+\frac{1}{2m}(\hbar k_y - eBx)^2\right]\varphi(x) = E\varphi(x), \tag{3.4}$$

which may be

$$\left[-\frac{\hbar^2}{2m}\left(\frac{\mathrm{d}^2}{\mathrm{d}x^2}\right)+\frac{1}{2}m\left(\frac{eB}{m}\right)^2\left(\frac{\hbar k_y}{eB} - x\right)^2\right]\varphi(x) = E\varphi(x). \tag{3.5}$$

This equation obviously resembles the one describing the one-dimensional harmonic quantum oscillator

$$\left[-\frac{\hbar^2}{2m}\left(\frac{\mathrm{d}^2}{\mathrm{d}x^2}\right)+\frac{1}{2}m\omega_c^2(x - x_0)^2\right]\varphi(x) = E\varphi(x), \tag{3.6}$$

centred at $x_0 = \hbar k_y/eB$, where $\omega_c = eB/m$ is the cyclotron frequency. The energy spectrum of such system is then expressed as

$$E_n = \left(n + \frac{1}{2}\right)\hbar\omega_c = (2n+1)B\frac{e\hbar}{2m}, \tag{3.7}$$

where the optical transitions between the Landau levels are governed by selection rules for different light polarizations:
(A) $n \to n+1$ for σ_- polarization (right circular)
(B) $n \to n-1$ for σ_+ polarization (left circular).

Due to these rules, all transitions are restricted only to the adjacent energy levels. The plot of the Landau energy spectrum—so called Landau fan—is depicted in the Fig. 3.1, where we can also see the characteristic linear scaling of cyclotron resonance with growing B.

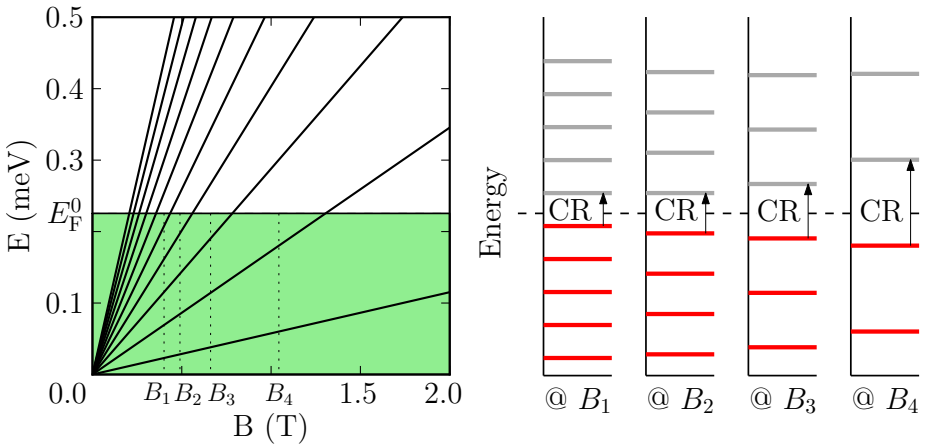

Fig. 3.1: Left: The plot of the Landau level spectrum for a gas of free electrons with a parabolic dispersion. The E_F^0 is Fermi energy of the system at zero magnetic field. Right: Energy levels at four different magnetic fields. The intraband excitations, so-called cyclotron resonance (CR), are possible only between adjacent levels. Adjacent levels are separated by the cyclotron energy $\hbar\omega_c$, where ω_c stands for classically defined cyclotron frequency $\omega_c = eB/m$. The red levels are completely filled with electrons whereas the grey levels are empty.

3.2 Landau levels in Dirac system

For characterization of the linearly dispersed surface states of Bi_2Se_3 in magnetic field we shall employ the basic Hamiltonian for massless Dirac electrons as it is sufficient enough to describe such a system in the similar way as in the graphene [46, 47]. For the sake of simplicity we also omit the Zeeman spin splitting in the model.

We assume the same field vector potential $\vec{A} = (0, Bx, 0)$ as in previous case, generating the same magnetic field $\vec{B} = (0, 0, B)$.

$$\hat{H} = v_F[p_x\sigma_x + (p_y - eBx)\sigma_y] = v_F \begin{pmatrix} 0 & p_x - ip_y + ieBx \\ p_x + ip_y - ieBx & 0 \end{pmatrix} \tag{3.8}$$

This time we solve the $\hat{H}\Psi = E\Psi$, where Ψ is now two-component spinor and σ_x, σ_y are Pauli matrices. One way how to find eigenvectors and corresponding eigenvalues is to solve the "squared" Schrödinger equation $\hat{H}^2\Psi = E^2\Psi$.[1]

$$\hat{H}^{\,2}\Psi = v_F^2[p_x\sigma_x + (p_y - eBx)\sigma_y][p_x\sigma_x + (p_y - eBx)\sigma_y]\Psi = \tag{3.9}$$

$$= v_F^2[p_x^2\mathbb{I}_2 + (p_y - eBx)^2\mathbb{I}_2 - \hbar eB\sigma_z]\Psi = E^2\Psi \tag{3.10}$$

[1]Note that an eigenstate Ψ of $\hat{H}$ is an eigenstate of $\hat{H}^{\,2}$, but not vice versa. In general, eigenvectors of $\hat{H}^2$ with eigenvalue E^2 do span the eigensubspaces of $\hat{H}$ corresponding to $\pm E$.

Here we used anticommutation relation $\{\sigma_i, \sigma_j\} = 2\delta_{i,j}\mathbb{I}_2$ (where $\mathbb{I}_2$ is 2×2 identity matrix) and also commutation relation $[x, p_x] = i\hbar$. Now we make the ansatz again $\Psi(\vec{r}) = \varphi(x)\mathrm{e}^{ik_y y}$ and obtain

$$\left[p_x^2 + e^2B^2\left(\frac{\hbar k_y}{eB} - x\right)^2\right]\mathbb{I}_2\varphi(x) = \left(\frac{E^2}{v_\mathrm{F}^2}\mathbb{I}_2 + \hbar eB\sigma_z\right)\varphi(x). \tag{3.11}$$

This is the equation of shifted quantum harmonic oscillator, this time, however, with the spectrum of eigenvalues reading

$$E_n = \mathrm{sgn}(n)v_\mathrm{F}\sqrt{2\hbar eB|n|} \qquad n = 0, \pm1, \pm2, ... \tag{3.12}$$

In contrast to the previously discussed case of massive particles with the Landau level spectrum scaling linearly with B, here we get the spectrum proportional to $\sqrt{B}$ (see Fig.3.2). Such a dependence usually serves as a hallmark of massless particles.

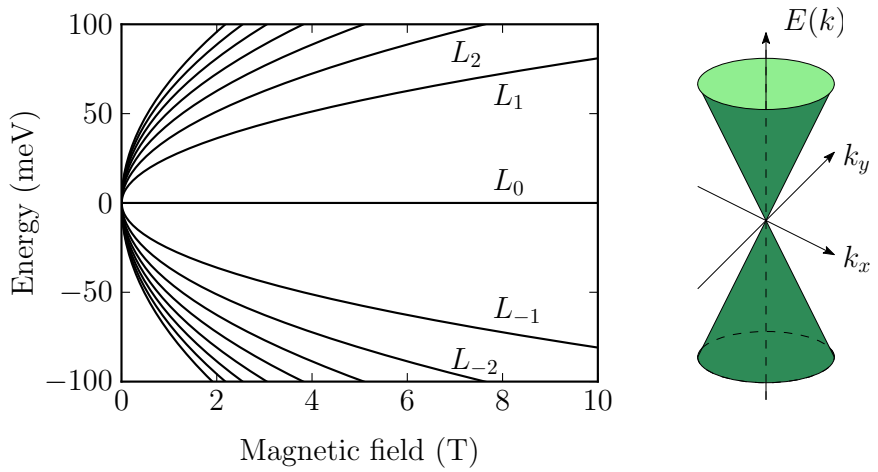

Fig. 3.2: Characteristic $\sqrt{B}$ dependence of Landau levels in the vicinity of Dirac point for a few low-index levels.

3.2.1 Magneto-optical response in Dirac system

To derive a simple model of magneto-optical response, we shall approximate the system as a 2DEG located between vacuum and dispersionless polar medium (Al_2O_3), which is described by refractive index n. The magneto-transmission of such a system can then be expressed as [48]:

$$T_\pm(\omega, B) = \frac{16n^2}{|\alpha_\pm|^2 - |\beta_\pm|^2}, \qquad \text{where} \qquad \begin{aligned}\alpha_\pm &= (n+1)[n+1+\sigma_\pm(\omega, B)] \\ \beta_\pm &= (n-1)[n-1-\sigma_\pm(\omega, B)],\end{aligned} \tag{3.13}$$

where $\sigma_{\pm}(\omega, B) = \sigma_{xx}(\omega, B) + i\sigma_{xy}(\omega, B)$ is the dynamical conductivity. The (–) and (+) signs denote right- and left-handed circular polarization. In the limit of weak absorption and normalised by the transmission of a substrate without the 2DEG, (3.13) may be further simplified to

$$T_{\pm}(\omega, B) \approx 1 - \frac{(n^2+3)}{2(n^2+1)} \frac{\mathrm{Re}[\sigma_{\pm}(\omega, B)]}{\epsilon_0 c}, \tag{3.14}$$

where ϵ_0 is vacuum permittivity and c is the speed of light. As obtaining the exact form for dynamical conductivity of Bi_2Se_3 in magnetic field might be rather complicated procedure, we use the well-known result of the linear-response theory, so-called Kubo-Greenwood formula [45, 48]:

$$\sigma_{\pm}(\omega, B) = \frac{2e^2}{\omega} \frac{|eB|}{h} \sum_{m,n} \frac{(f_n - f_m)}{E_m - E_n - (\hbar\omega + i\gamma)} \langle n|\hat{v}_{\pm}|m\rangle\langle m|\hat{v}^*_{\pm}|n\rangle \tag{3.15}$$

$$\mathbb{R}\mathrm{e}[\sigma_{\pm}(\omega, B)] = \frac{2e^2}{\omega} \frac{|eB|}{h} \sum_{m,n} \frac{(f_n - f_m)}{(E_m - E_n - \hbar\omega)^2 + \gamma^2} |\langle n|\hat{v}_{\pm}|m\rangle|^2. \tag{3.16}$$

Here E_m, E_n are energies of the m, n Landau levels, and $0 < f_m, f_n < 1$ represent the occupancies of said levels described by Fermi-Dirac distributions. The factor γ here denotes phenomenological line broadening and $\hat{v}_{\pm} = 1/\sqrt{2}(\hat{v}_x \pm i\hat{v}_y)$ are velocity operators.

To proceed further, we calculate the matrix elements in (3.16) which are governing the optical transition rules of the system. The wavefunctions corresponding to the Landau levels can be expressed as

$$\Phi_n = \frac{1}{\sqrt{2}} \begin{pmatrix} \mathrm{sgn}(n) h_{|n|-1} \\ h_{|n|} \end{pmatrix} \tag{3.17}$$

where the functions $h_n(x, y)$ are defined as

$$h_n(x, y) = \frac{(a^\dagger)^n}{\sqrt{n!}} h_0(x, y) \tag{3.18}$$

The lowering and raising operators are given by

$$\hat{a} = \left(\sqrt{\frac{\hbar}{2eB}}\right)(\hat{\pi}_x - i\hat{\pi}_y) \qquad \hat{a}^\dagger = \left(\sqrt{\frac{\hbar}{2eB}}\right)(\hat{\pi}_x + i\hat{\pi}_y). \tag{3.19}$$

Here $\hat{\pi}_x = -i\partial/\partial x + e/\hbar A_x$ and $\hat{\pi}_y = -i\partial/\partial y + e/\hbar A_y$. We can now rewrite the Hamiltonian for Dirac particles in magnetic field to

$$\hat{H}_0 = v_{\mathrm{F}}\sqrt{2e\hbar B}\begin{pmatrix} 0 & \hat{a} \\ \hat{a}^\dagger & 0 \end{pmatrix} = E_1 \begin{pmatrix} 0 & \hat{a} \\ \hat{a}^\dagger & 0 \end{pmatrix}, \tag{3.20}$$

where the E_1 denotes the energy of first Landau level. Using Hamiltonian in this form, we can then define the velocity operators as commutators

$$\hat{v}_x = \frac{1}{i\hbar}[x, \hat{H}] = v_{\mathrm{F}} \begin{pmatrix} 0 & 1 \\ 1 & 0 \end{pmatrix}, \qquad \hat{v}_y = \frac{1}{i\hbar}[y, \hat{H}] = v_{\mathrm{F}} \begin{pmatrix} 0 & -i \\ i & 0 \end{pmatrix} \tag{3.21}$$

Now after we defined the velocity operators, one can calculate the matrix elements in (3.16) formula to

$$\langle n|\hat{v}_+|m\rangle\langle m|\hat{v}_+^*|n\rangle = v_{\mathrm{F}}^2 h_{|n|-1}^2 h_{|m|}^2 = \frac{v_{\mathrm{F}}^2}{2}\delta_{|n|-1,|m|} \tag{3.22}$$

$$\langle n|\hat{v}_-|m\rangle\langle m|\hat{v}_-^*|n\rangle = v_{\mathrm{F}}^2 h_{|n|}^2 h_{|m|-1}^2 = \frac{v_{\mathrm{F}}^2}{2}\delta_{|n|,|m|-1} \tag{3.23}$$

The optical selection rules then allow inter-LL transitions from $L_n \to L_m$ for $|m| = |n| - 1$ for (+) light polarization and $|m| = |n| + 1$ for (–) light polarization (see Fig. 3.3). In general, there are three different groups of possible transitions ($i \geq 1$):

(A) *Interband* resonances $L_{-i} \to L_{i+1}$ and $L_{-i-1} \to L_i$ at energy $E_1(\sqrt{|i|+1}+\sqrt{|i|})$
(B) *Intraband* resonances $L_i \to L_{i+1}$ and $L_{-i-1} \to L_{-i}$ at energy $E_1(\sqrt{|i|+1}-\sqrt{|i|})$
(C) Mixed resonance $L_{-1} \to L_0$ and $L_0 \to L_1$ at energy E_1 involving the 0th LL.

These transitions are very different compared to those in conventional 2DEG, as they are no more limited only to adjacent levels. In practise, the intraband transitions are usually referred to as cyclotron resonance absorption, and they are found in spectra at lower energies as compared to the interband transitions.

If we take into account non-polarized light, the transitions are simply those between states n, m such that $|m| = |n| \pm 1$. Using non-polarized light, as in our experiment, it is not possible to distinguish between transitions where the indices n and m have different signs, i.e. for example transitions $L_{-1} \to L_0$ and $L_0 \to L_{-1}$ or transitions $L_{-1} \to L_2$ and $L_{-2} \to L_1$. For this case the relation (3.15) can be rewritten as

$$T(\omega, B) = \frac{1}{2}[T_+(\omega, B) + T_-(\omega, B)] \approx 1 - \frac{(n^2+3)}{2(n^2+1)}\frac{\mathbb{R}\mathrm{e}[\sigma_{xx}(\omega, B)]}{\epsilon_0 c} \tag{3.24}$$

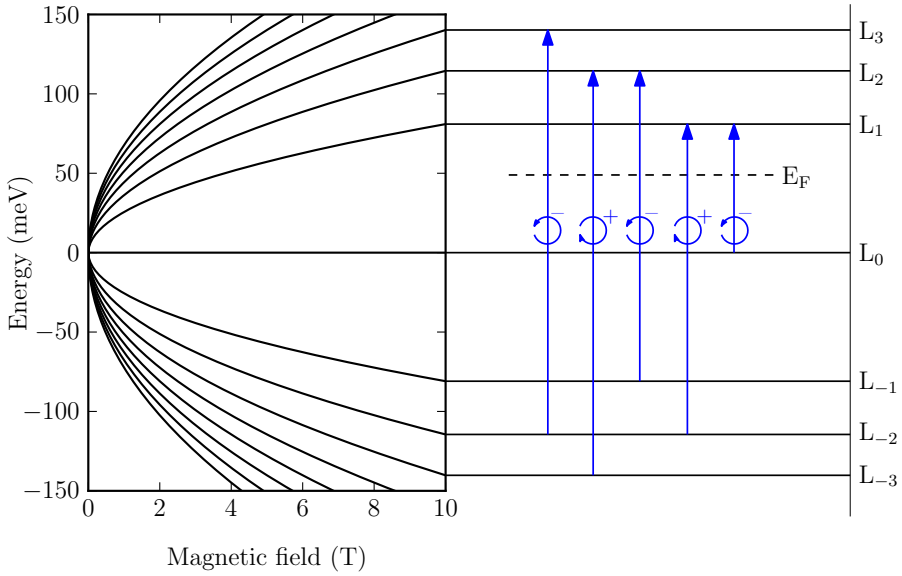

Fig. 3.3: The fan diagram showing Landau level spectrum of a Dirac electrons and few selected electric-dipole-active transitions with corresponding polarizations at 10 T. Adapted from [45].

In the quantum limit of high magnetic fields, i.e. where all electrons are occupying only the L_0 level, and for line broadening small compared to the energy of transition, the transmission for a single transition can be further approximated to

$$T(B) = \frac{(n^2+3)}{2(n^2+1)} \frac{e^2}{2\epsilon_0 \hbar c} E_1 = \frac{(n^2+3)}{2(n^2+1)} \frac{e^2}{2\epsilon_0 \hbar c} v_\mathrm{F} \sqrt{2e\hbar B} \tag{3.25}$$

This linear in $\sqrt{B}$ transmission dependence is generally important feature of magneto-optical spectra as it is the key evidence of Dirac system. Furthermore, as the Fermi velocity v_F is the only free parameter, one can easily calculate its value from the $\sqrt{Bn}$ slope of the transmission spectra.

3.2.2 Quasi-classical approach to cyclotron resonance

Applying magnetic field of only a few Tesla on the Dirac system described above will result in not fully resolved spectrum of Landau levels (see Fig. 3.4) as the intraband transitions near Fermi energy are packed quite tightly together, thus indistinguishable. Limiting ourselves only to this low-field regime, it is possible to describe the cyclotron resonance using simple quasi-classical formalism [49].

First lets expand the relation for energy of intraband transitions to

$$\hbar\omega_c = v_\mathrm{F} \sqrt{2e\hbar B} (\sqrt{n+1} - \sqrt{n}) \cdot \frac{\sqrt{n+1} + \sqrt{n}}{\sqrt{n+1} + \sqrt{n}}. \tag{3.26}$$

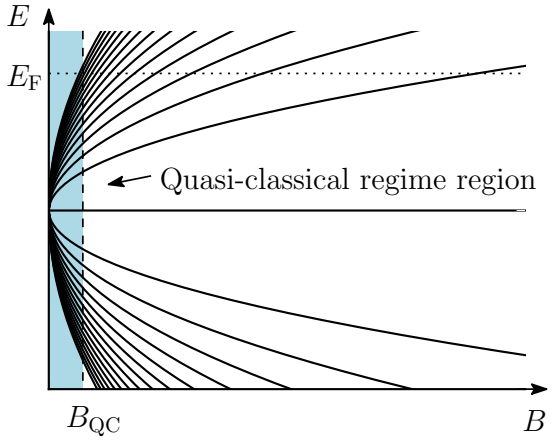

Fig. 3.4: The Landau level spectrum fan diagram with highlited approximative region, where the quasi-classical characterization of the system still holds.

In the low-field limit, the intraband transitions around E_F are generally realized at levels with large indices n. Following this, we can approximate $\sqrt{n+1} \approx \sqrt{n}$ and rewrite the equation above to

$$\hbar\omega_c = v_\mathrm{F}\sqrt{2e\hbar B} \cdot \frac{1}{2\sqrt{n}}. \tag{3.27}$$

We then substitute $\sqrt{n}$ from the relation for $E_\mathrm{F} = v_\mathrm{F}\sqrt{2e\hbar Bn}$ giving us

$$\hbar\omega_c = v_\mathrm{F}\sqrt{2e\hbar B} \cdot \frac{1}{2} \cdot \frac{v_\mathrm{F}\sqrt{2e\hbar B}}{E_\mathrm{F}} = \frac{e\hbar B}{(E_\mathrm{F}/v_\mathrm{F}^2)}, \tag{3.28}$$

where $E_\mathrm{F}/v_\mathrm{F}^2$ is defined as a energy dependent cyclotron mass m. Such relation $E_\mathrm{F} = mv_\mathrm{F}^2$ is equivalent to the very well known Einstein relation between mass and energy, reflecting the relativistic character of electronic states in massless Dirac system. As we can see, the cyclotron resonance in the low-field limit depends linearly on B in the similar way like the 2DEG with parabolic dispersion.

Moving on the optical response in quasi-classical regime, we employ the same mechanism as in the formula (3.13). Here, however, the dynamical conductivity for (+) and (−) polarization is given by

$$\sigma_\pm(\omega, B) = \sigma_0 \frac{i\gamma}{\omega \pm \omega_c + i\gamma}, \tag{3.29}$$

where σ_0 is zero-field DC conductivity, γ again represents the line broadening and $\omega_c = eB/m$. For simplicity, here we assume no field dependency of both γ and σ_0, as they are later used as fitting parameters.

To get relative transmission lines in case of using non-polarized light, we average the transmission for both polarizations and divide by transmission in zero magnetic field

$$T_{rel}(\omega, B) = \frac{T_+(\omega, B) + T_-(\omega, B)}{2T(\omega, 0)}. \tag{3.30}$$

Clearly linear relative transmission spectra at field up to 10 T are illustrated in Fig. 3.5, where we modelled the quasi-classical optical response. When fitting the data using this model, one has to realize that due to line broadening, the dip in the relative transmission spectra is not exactly in the same position as the actual cyclotron resonance mode (although the margin of this error is quite small, see left part of Fig. 3.5).

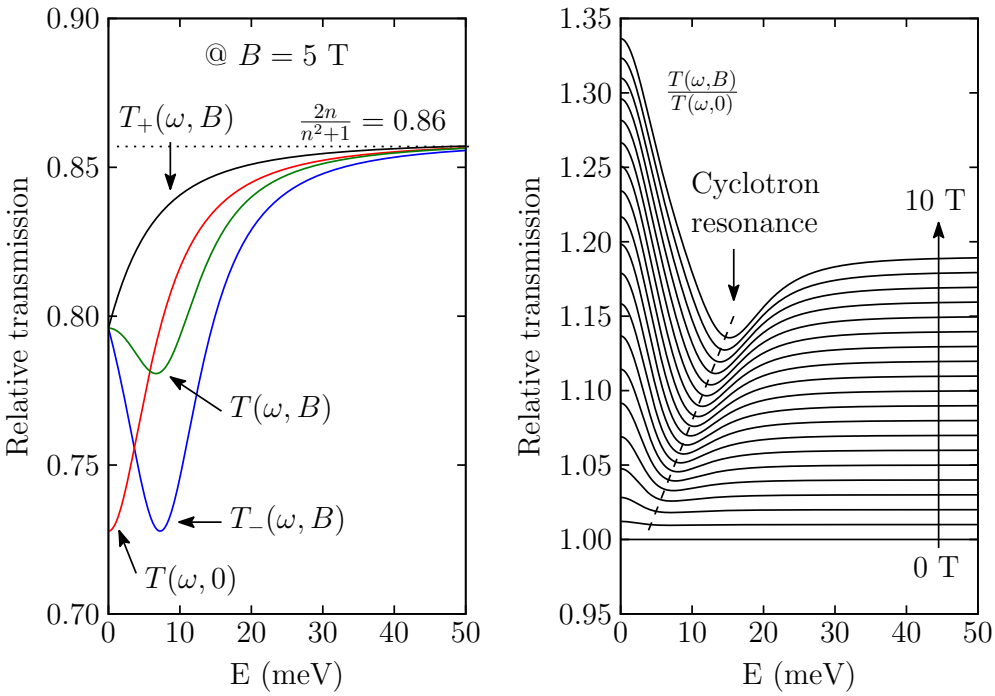

Fig. 3.5: Left: Plot of the modelled component terms from (3.30) in the magnetic field 5 T demonstrates individual contributions to the final relative transmission. The common limit is derived from transmission of dielectric slab without any conducting layer, i.e. $\sigma_\pm(\omega, B) = 0$. The slab is represented by Al_2O_3 substrate with $n = 1.76$ Right: Modelled relative transmission spectra at fields from 0 T to 10 T with indicated broad linear in B cyclotron resonance. The spectra are shifted by 0.01 for clarity.

4 INSTRUMENTATION FOR INFRARED SPECTROSCOPY IN MAGNETIC FIELD

Studying the optical response of electronic systems in magnetic fields requires relatively specific experimental apparatus. Since a number of magneto-optical experiments requires (due to specific system properties or simply due to insufficient electronic quality) the application of magnetic fields reaching several tesla or more, it is essential to build powerful installations capable of delivering such high magnetic fields, where we can operate the infrared spectroscopic technique. One such facility meeting these requirements is the IR laboratory at *Laboratoire National de Champs Magnétiques Intenses* (LNCMI) in Grenoble capable of realizing experiments in magnetic fields as high as 35 T.

The following chapter explains the basic principles of the FTIR spectroscopy and also provides the description of the magnetic devices used at LNCMI.

4.1 Fourier transform infrared spectroscope

One of the instruments of the experimental setup is the IR spectroscope *Bruker Optics - IFS 66v/S* which is able to perform measurements in the full IR range, that is from far-infrared $\sim$20 cm^{-1} almost up to ultraviolet (UV) $\sim$40 000 cm^{-1} depending on the installed extensions [50]. To get an insight of the inner workings of such spectroscope, we will now describe the three essential components.

4.1.1 Source of IR light

As the infrared portion of the electromagnetic spectrum is usually divided into three regions; the near-infrared (NIR), mid-infrared (MIR) and far-infrared (FIR), so are also the types of IR sources. Starting first with MIR, the ideal source of continuous mid-infrared radiation is a high-temperature black-body. The spectral radiance from a blackbody source as a function of wavenumber ν and temperature T, is given by the Planck equation

$$U(\nu, T) = \frac{2h\nu^3}{c^2} \frac{1}{e^{h\nu/kT} - 1}, \tag{4.1}$$

which is plotted for a different temperatures in Fig. 4.1. At first glance, one can say that the maximum of emission follows the Wien law and one has to chose right temperature for a given spectral region. This is not always the case, however. For example, the temperature of a tungsten filament in a standard incandescent light

bulb is close to 3000 K, but tungsten filaments are sealed in a glass bulb so that they can be operated under a high vacuum.

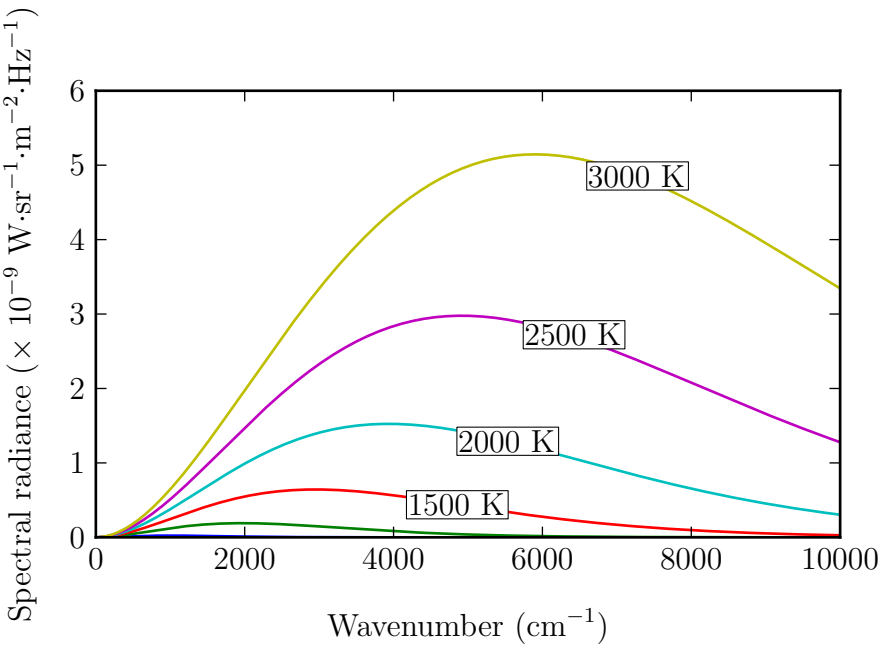

Fig. 4.1: Plot of the Planck law for black body for a selected temperatures.

The most common mid-infrared source used in FT-IR spectrometers is a resistively heated silicon carbide rod, commercially known as a Globar^{TM}. The typical temperature at which a Globar is operated is ∼1300 K. In the past, Globars were always water-cooled to avoid overheating the electrical contacts, but some ceramic sources are now available that can be run without the need for a source of cooling water; however, these are generally operated at a lower temperature.

Considering the NIR sources, it can be inferred from Fig. 4.1 that they should be run at significantly higher temperatures than mid-infrared sources. Since glass and quartz are transparent across the entire NIR region, this goal can be met through the use of a simple and inexpensive tungsten-filament light bulb or quartz-tungsten-halogen (QTH) lamp. Provided that these sources are run at less than their specified operating voltage, they are also very long lived [51].

The spectral radiance in Fig. 4.1 also tells us that the spectral radiance of blackbody sources is always very low below 200 cm^{-1} and the problem of measuring far-infrared spectra is also related to the fact that the emissivity i.e. thermal radiation efficiency of Globar is much less than unity in the far infrared. Since the sensitivity of any measurement of a MIR or FIR spectrum is directly proportional to the spectral radiance of the source, it is apparent that far-infrared sources should be as hot as possible. It is therefore customary to use a high-pressure mercury lamp

for measurements between $\sim$50 cm^{-1} and the onset of the microwave region of the spectrum. The reason why mercury lamps have proved to be so successful for far-infrared spectrometry is because emission from the plasma reinforces the emission from the hot quartz envelope of the lamp. However, the mercury lamp has significant flicker noise, so even if the energy is better, the signal-to-noise ratio may not always be.

Last but not least, the ultimate FIR source providing high brightness, high flux (very good signal-to-noise ratio) and small divergence of the beam is the synchrotron. Such qualities however come at price—synchrotrons are usually very large and complex installations which is then reflected on the general availability of such sources for experiments.

4.1.2 Detectors

Quantum detectors

In general the IR detectors can be divided into two classes—quantum detectors and thermal detectors. Quantum detectors operate on the basic principle of excitation of electrons to different electronic state by incoming light. One way is a photoemission, where electrons are given enough energy to escape from the surface and flow through a vacuum to produce an electrical current. Phototubes and photomultipliers fall into this category. Because high energies are required to release electrons from a photoemissive surface, this effect can only be used in the ultraviolet, visible, and NIR (up to the wavelengths of 1 µm) regions.

Semiconductor detectors, where the radiation is generally absorbed on a p-n junction, are often used in the mid- and near-infrared range. Quantum detectors that operate in this manner include, for instance, PbS, PbSe, and InSb [52]. Other quantum detectors include II–VI combinations of semimetals and semiconductors, that is, mixtures of metals and semiconductors from groups II and VI of the periodic table. One such detector is also already discussed mercury cadmium telluride (MCT, $Hg_{1-x}Cd_xTe$), where the ratio of the blend leads to the bandpass of the detector (3 - 30µm) [52]. MCT detectors are by far the most commonly used photo-detectors for mid-infrared spectrometry. Semiconductor detectors in general exhibit both perfect signal-to-noise performance and a very fast response.

However, the very low energy of the photons that must be sensed by MIR photodetectors has the consequence that electrons can be excited by random thermal fluctuation of the solid, which gives rise to noise in the output. Noise is also generated by leakage of current through the detector from the photoconductive or photovoltaic circuit used to bias the detector. Thus, cryogenic cooling is usually used to reduce these sources of noise, which adds to complexity of the experimental setup.

Thermal detectors

The second group—thermal detectors—works on the principle that the absorbed incident radiation changes the temperature of the material, and the resulting change in some physical properties is used to generate electrical output. Their output may be in the form of an electromotive force (e.g., thermocouples), a change in the resistance of a conductor (e.g., bolometers) or semiconductor (e.g., thermistor bolometers), or the movement of a diaphragm caused by the expansion of a gas (e.g., pneumatic detectors). All of the above types of thermal detectors have been used for mid-infrared measurements. They all have drawbacks for FTIR spectroscopy, since each has a response time of several milliseconds.

Although several cryogenically cooled detectors have low response times, the only mid-infrared detectors that have an appropriate combination of high speed, reasonably good sensitivity, low cost, good linearity, and operation at or near room temperature are the pyroelectric bolometers. In these devices, the key component responsible for registering the heat difference is ferroelectric material that exhibits a large spontaneous electrical polarization at temperatures below their Curie point. If the temperature of these materials is changed, the degree of polarization is changed, and this can be registered as an electrical signal if electrodes are placed on the sides of thin slab of material to form a capacitor.

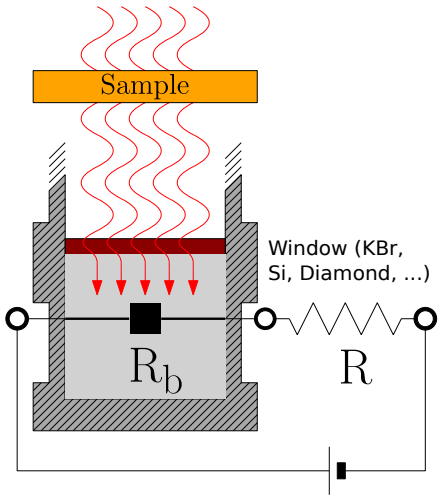

Fig. 4.2: Simplified schematics of DTGS pyroelectric bolometer. By changing the R_b by light, applied (constant) voltage on R_b and R is redistributed and the voltage variation on R_b or R (depends on which we follow electrically) is registered as a signal.

For such devices, the most commonly used material is deuterated triglycine sulfate (DTGS) [51]. It is important to mount the DTGS so that the thermal resistance

between the slab and its environment is sufficiently large. This is usually achieved by suspension of DTGS on thin copper wires in evacuated cavity as seen in Fig. 4.2.

In previous section was hinted that the intensity of FIR radiation emitted by most sources is rather low. Therefore spectra in this range measured using pyroelectric bolometer have often high noise-to-signal ratio. Solution to this problem are liquid helium cooled bolometers.

4.1.3 Michelson interferometer

Although there exists a number of different interferometer designs, most of them are based on the two-beam type introduced by Albert A. Michelson at the end of 19^{th} century. The Michelson interferometer is a device that can divide a beam of radiation into two paths and then combine the two beams after a path difference has been introduced (see Fig. 4.3). The difference between the two branches of the interferometer then results in the interference of recombined beams, altering the intensity of outcoming light.

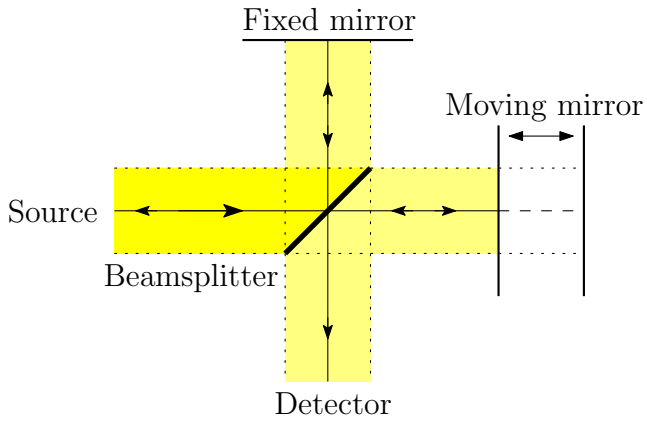

Fig. 4.3: Schematic layout of Michelson interferometer. It consists of two mutually perpendicular plane mirrors, one of which can move along an axis that is perpendicular to its plane.

To understand the processes that occur in a Michelson interferometer better, let us first consider an idealized situation where a source of monochromatic radiation produces an infinitely narrow, perfectly collimated beam. Instead in terms of radiation wavelength λ_0, we shall work with its wavenumber $\tilde{\nu}_0 = 1/\lambda_0$ (in cm^{-1}) so then we can then denote the radiation intensity, or interference record, $\overline{I}$ at detector as follows

$$\overline{I}(\Delta) = 0.5I(\tilde{\nu}_0)[1 + \cos(2\pi\tilde{\nu}_0\Delta)]. \tag{4.2}$$

Here the Δ is the path difference or retardation of the beams and $I(\tilde{\nu}_0)$ is the intensity of the source. One can see that the intensity $\overline{I}(\Delta)$ is composed of constant DC part $0.5I(\tilde{\nu}_0)$ and modulated AC part $0.5I(\tilde{\nu}_0)\cos(2\pi\tilde{\nu}_0\Delta)$. Only the AC component is important in spectrometric measurements, and it is this modulated component that is generally referred to as the interferogram

$$I(\Delta) = \frac{1}{2} I(\tilde{\nu}_0)\cos(2\pi\tilde{\nu}_0\Delta) \tag{4.3}$$

In practice, several factors affect the magnitude of the signal measured at the detector. First, it is practically impossible to find a beamsplitter that has the ideal characteristics of 50% reflection and 50% transmission [51]. The nonideality of the beamsplitter must be allowed in (4.3) by multiplying $I(\tilde{\nu}_0)$ by a wavenumber-dependent factor of less than unity that represents the relative beamsplitter efficiency. Another issue rises from the fact, that most of the infrared detectors do not exhibit uniform response at all wavenumbers. In addition, the response of many signal amplifiers is also strongly dependent on the modulation frequency. So, to take in account all these effects, the (4.3) can be rewritten to

$$I(\Delta) = \frac{1}{2} B(\tilde{\nu}_0)H(\tilde{\nu}_0)\, I(\tilde{\nu}_0)\cos(2\pi\tilde{\nu}_0\Delta) = A(\tilde{\nu}_0)\cos(2\pi\tilde{\nu}_0\Delta), \tag{4.4}$$

where $B(\tilde{\nu}_0)$ represents the beam beamsplitter efficiency, and $H(\tilde{\nu}_0)$ is efficiency coming from detector and amplifier response. Of all factors in the equation above, only $I(\tilde{\nu}_0)$ varies from one measurement to the next for a given system configuration, while all the other factors remain constant. For clarity, we can combine all factors into one factor $A(\tilde{\nu}_0)$.

So far, we considered only the monochromatic source of light. When radiation of more than one wavelength is emitted by the source, the measured interferogram may be view as a sum (integral) of the interferograms that correspond to each wavelength. If we now consider a source with continuous spectrum of radiated light, the (4.4) can be expressed as

$$I(\Delta) = \int_{-\infty}^{\infty} A(\tilde{\nu})\cos(2\pi\tilde{\nu}\Delta)\,\mathrm{d}\tilde{\nu}, \tag{4.5}$$

which is the form of cosine Fourier transform. To express the $A(\tilde{\nu})$, we shall employ the inverse cosine Fourier transform

$$A(\tilde{\nu}) = \int_{-\infty}^{\infty} I(\Delta)\cos(2\pi\tilde{\nu}\Delta)\,\mathrm{d}\Delta, \tag{4.6}$$

which will provide us with a frequency spectra of the interferogram (see Fig. 4.4).

The mathematical apparatus of Fourier transform (FT) stands at the very core of this spectroscopic technique, hence the name *Fourier transform infrared spectroscopy*. Today, most of the crude computation is done by less time-consuming algorithms including the most widely used Fast Fourier transform.

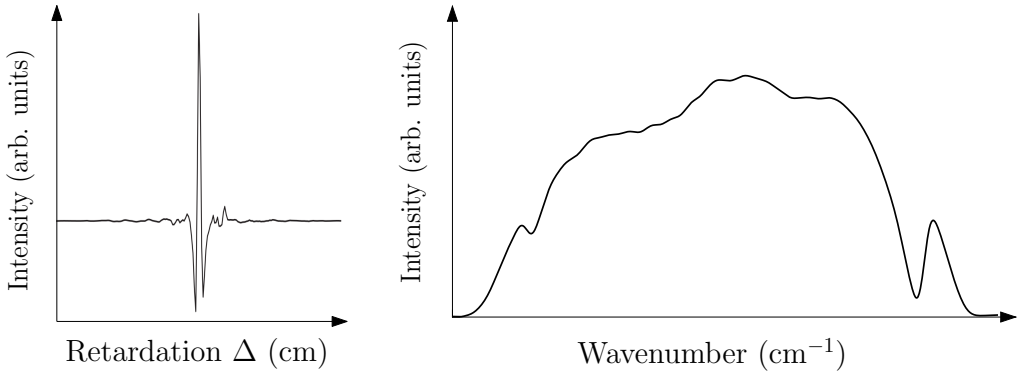

Fig. 4.4: Applying Fourier transform on typical interferogram (left) retrieved from Michelson interferometer allows one can to calculate the wavenumber spectra (right).

To obtain very precise results from the FT, it is important to ensure very smooth movement of a scanning mirror without any tilting. For this reason, the technical solution of the mirror in the Michelson interferometer can be realized, for example, using an electromagnetic drive and an air bearing.

4.2 Magnetic field installation

As mentioned earlier, the magneto-optical experiments were performed both at low magnetic field provided by superconducting coil and at high magnetic field provided by one of the several water-cooled resistive magnets at the facility. We will now discuss the difference in their designs and field strength.

4.2.1 Superconductive coil

The preliminary transmission spectra were first measured in helium cooled superconducting coil, which is nominally operated at 4.2 K at atmospheric pressure. At these conditions, the maximum magnetic field is 11 T. The field can be further enhanced to 13 T when the helium bath is pumped down to temperature below 2.2 K.

The bore of the magnet, indicating the diameter of the hole in the middle of a solenoid, is important parameter for experiment design as it significantly limits the dimensions of probe and therefore sample holder or potentially also LED and wiring

compartment. Usually the stronger the field, the smaller the bore diameter as the goal is better field focus (the magnet we used has the bore of 50 mm).

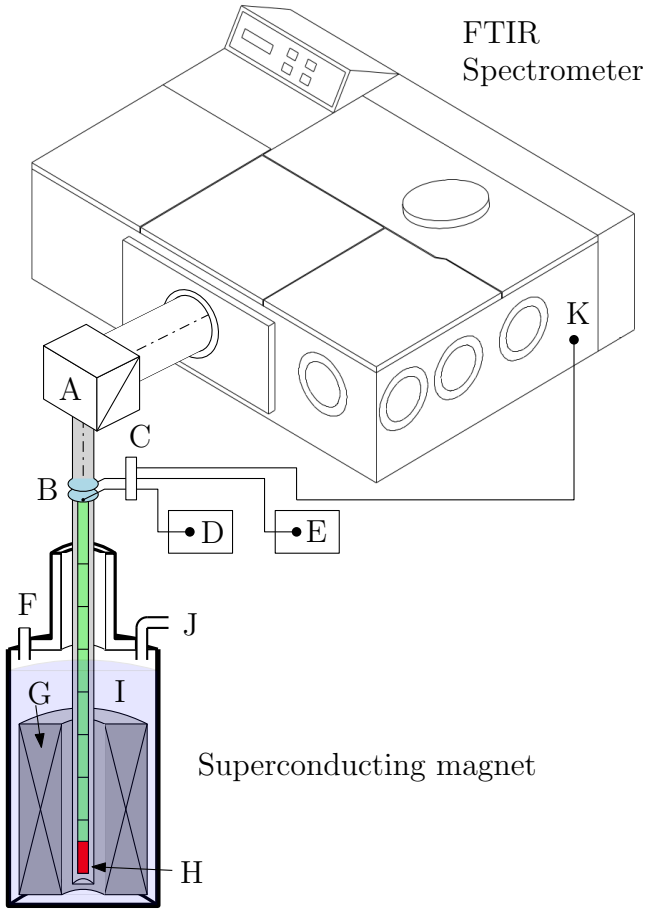

Fig. 4.5: Simplified schematics of magneto-optical experiment setup consisting of FTIR spectrometer and superconducting magnet. Individual parts are described in the text below.

To get better idea of setup layout see Fig. 4.5. The light beam from spectrometer is reflected by a custom golden-plated mirror (A) into the probe waveguide through polyethylene window (B). Up to this point, the light-path (including spectroscope) is evacuated, and the probe itself is sealed and filled with heat exchange gas (He at ∼30 mBar), ensuring gradual cooling of the probe. The top of the probe also contains signal port (C), where the output is the registered signal from the external bolometer under sample-holder (H). The bolometer is electrically polarized by the voltage from the DC source (D) and the signal from the bolometer is amplified (E) and sent to spectrometer signal input port (K). The cryostat (I) is usually filled with helium through the hole on top (F) using capillary transfer from Dewar bottle. The

evaporated helium is collected from the (J) port and sent to liquefier. This port is also used when the cryostat is being pumped out to reach lower temperatures (down to 1.6 K).

4.2.2 Resistive magnet

Performing experiments in more powerful resistive magnet yields quite different requirements for operating experimental setup. The magnet is capable of outputting stationary magnetic field of 35 T. The required DC electric power is supplied by four AC/DC power converters, each about 6 MW. These converters, based on SCR Rectifier Bridges (thyristors), provide up to 16 kA at 400 V with a current stability of about 10 ppm. They can also be connected in parallel on a single magnet for providing up to 64 kA [53].

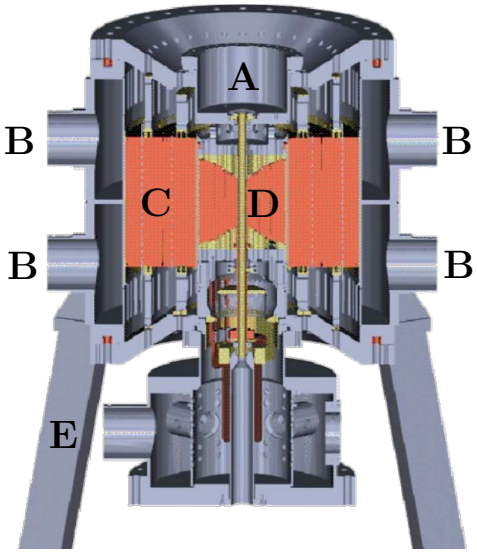

Fig. 4.6: Schematics of resistive magnet M9 at LNCMI Grenoble. The cryostat is inserted from the top of the construction (A) with the probe in the 34mm bore (D) of the coil (C). The cooling water is pumped through the inlets of the outer shell (B), whereas the the electric wiring is led through lower inlet (E).

Such high values of electric current necessarily create a large quantities of heat in the magnet coils. So the magnet is cooled down by a closed loop of deionised and deoxygenated water. For a magnet at peak 24 MW power, the typical water flow rate is about $300\,\mathrm{l}\cdot\mathrm{s}^{-1}$ with water temperature difference about 15 °C. A secondary circuit extracts the heat from the closed loop using a mechanical heat exchanger and the water from the neighbour river. Nevertheless, such a high water flow causes vibration of the platform which can influence the signal-to-noise ratio of experiments.

The probe itself is cooled in helium cryostat with liquid nitrogen jacket, which is inserted into the top of the magnet (see Fig. 4.6).

Another problem to consider is the connection between probe in magnet and spectrometer. As the field is significantly strong in a radius of a few meters from the magnet, all sensitive instruments have to be outside of the "danger zone" as well as all tools and parts from ferrous metals, otherwise they could be pulled towards the magnet and could potentially rupture the cryostat. The solution to this is using a 2 meters long waveguide connecting the probe with a spectroscope allowing safe measurements from distance.

Apart from different magnet type, different probe design and longer waveguide, the experimental setup is identical to the one in the low fields.

5 EXPERIMENTS AND RESULTS

As stated in section 2.4.1, we obtained, in total, four samples of Bi_2Se_3 heterostructure. All samples were characterized using low-field magneto-transmission technique. These experiments allowed us to choose the most promising sample for measurements in high magnetic field, using resistive coils at LNCMI. As the procedure of the probe preparation is more or less same for both fields, it will be briefly disclosed first.

All measurements were performed in the Faraday configuration—incident light was propagating in parallel to the applied magnetic field and the magnetic field was always oriented perpendicular to the sample. The samples (dimensions of all them were 10×10 mm^2) were glued to the sample holder over one of the two holes (see Fig. 5.1). The second hole serves as a source of reference spectra, which allows us to correct for the field-induced response of the bolometer (located inside the magnet, and therefore, strongly influenced by the magnetic field). Depending on the transmission signal strength from samples, the diameter of the holes can be replaced. The sample holder is then attached to the tip of the waveguide, which is also holding the rod for rotating the holder from "sample position" to "reference position".

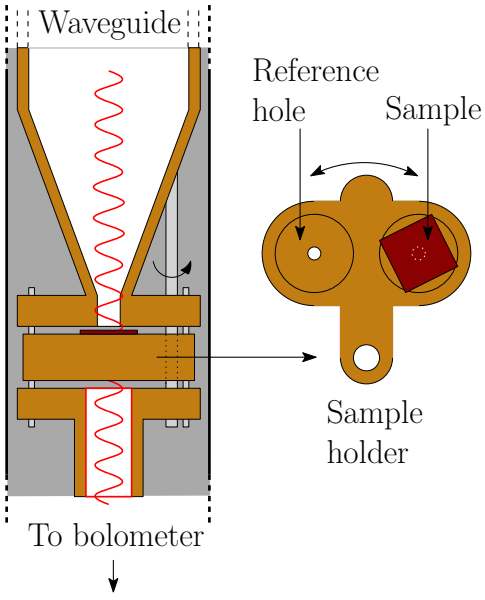

Fig. 5.1: Left: Schematic drawing of the sample holder in a probe for transmission measurement in Faraday configuration, where the light is guided from spectrometer through the sample to the bolometer. Right: detail of the sample holder with sample itself and hole for reference measurement.

Next, the bolometer is attached under the holder and signal wires (which are

fastened to the waveguide) are connected. The waveguide with attached sample holder and bolometer is then inserted into long metallic tube, hermetically sealed, evacuated and then filled with the helium gas with the pressure of ∼30 mbar. This probe is then inserted into the magnet slowly enough to reduce the risk of damaging the bolometer and sample by rapid cooling. After the probe is fully inserted, the waveguide between polyethylene window (chosen due to high transparency in the spectral range of interest) and spectrometer evacuated, and bolometer is cooled to liquid helium temperature, it is possible to start with spectra measurements.

5.1 Low-field magneto-transmission spectra

The following figures illustrate the relative magneto-transmission spectra at fields up to 11 T. In this range, the system can be described using the formalism introduced in section 3.2.2, implying the linear in B dependence of cyclotron resonance.

Indeed, the single-mode cyclotron resonance absorption mode, clearly visible in transmission spectra of all four samples, evolves linearly with B (see heatmaps in Fig. 5.2B – 5.5B). For the 6QL sample, the overall signal becomes relatively weak and the slope cannot be read-out with a reasonable precision, but still, the linear in B dependency may be guessed from the heat map.

In the model, we assumed that the cyclotron mass m, line broadening coefficient γ, and DC conductivity σ_0 are all independent of the applied magnetic field and can be used as fitting parameters. To simply fit the data with the model, the spectra first needed to be cut to relevant region of the cyclotron resonance energies 5 – 60 meV (see Fig.5.2A,B – 5.5A,B). The values extracted from the model are in Tab. 5.1 below.

Tab. 5.1: Deduced values of m, γ, and σ_0 obtained from quasi-classical model of relative transmission. The effective mass is compared to the mass obtained by Wu *et al.* from Faraday rotation experiments [54].

sample	γ (meV)	σ_0 ($10^{-3} \cdot \Omega^{-1}$)	m (m_e)	m_{Faraday} (m_e)
6QL	15.5 ± 2.1	0.16 ± 0.02	0.056 ± 0.009	0.045 ± 0.009
8QL	7.7 ± 1.7	0.26 ± 0.03	0.058 ± 0.008	0.061 ± 0.007
10QL	6.9 ± 1.3	0.35 ± 0.03	0.076 ± 0.007	0.068 ± 0.005
16QL	6.4 ± 1.6	0.60 ± 0.03	0.08 ± 0.01	0.077 ± 0.005

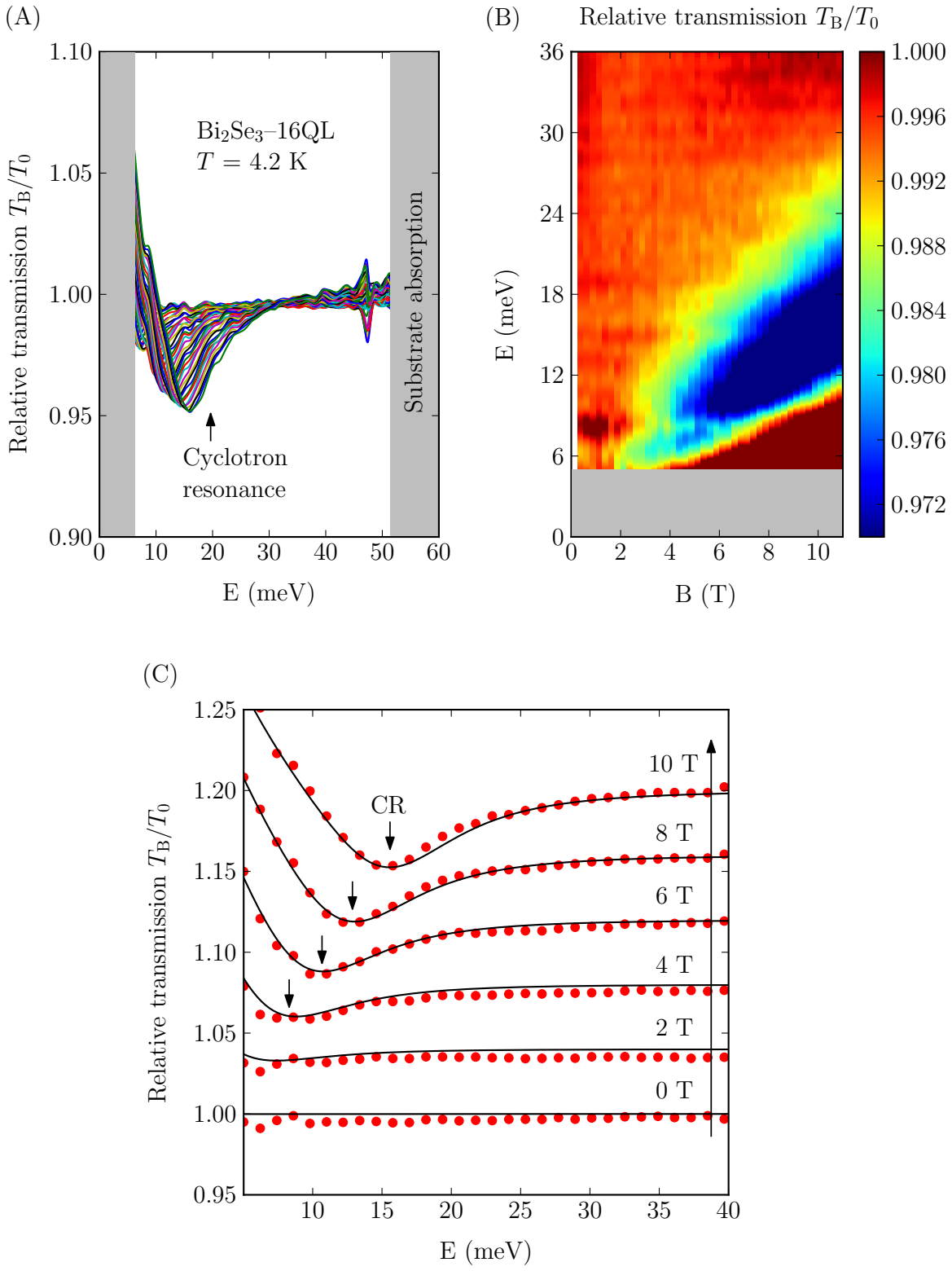

Fig. 5.2: Relative transmission of 16QL Bi_2Se_3 (A) represented also as a heatmap (B). The quasi-classical fit (lines) of the cyclotron resonance (marked by arrows) is depicted in (C) (the spectra are shifted by 0.04 for clarity).

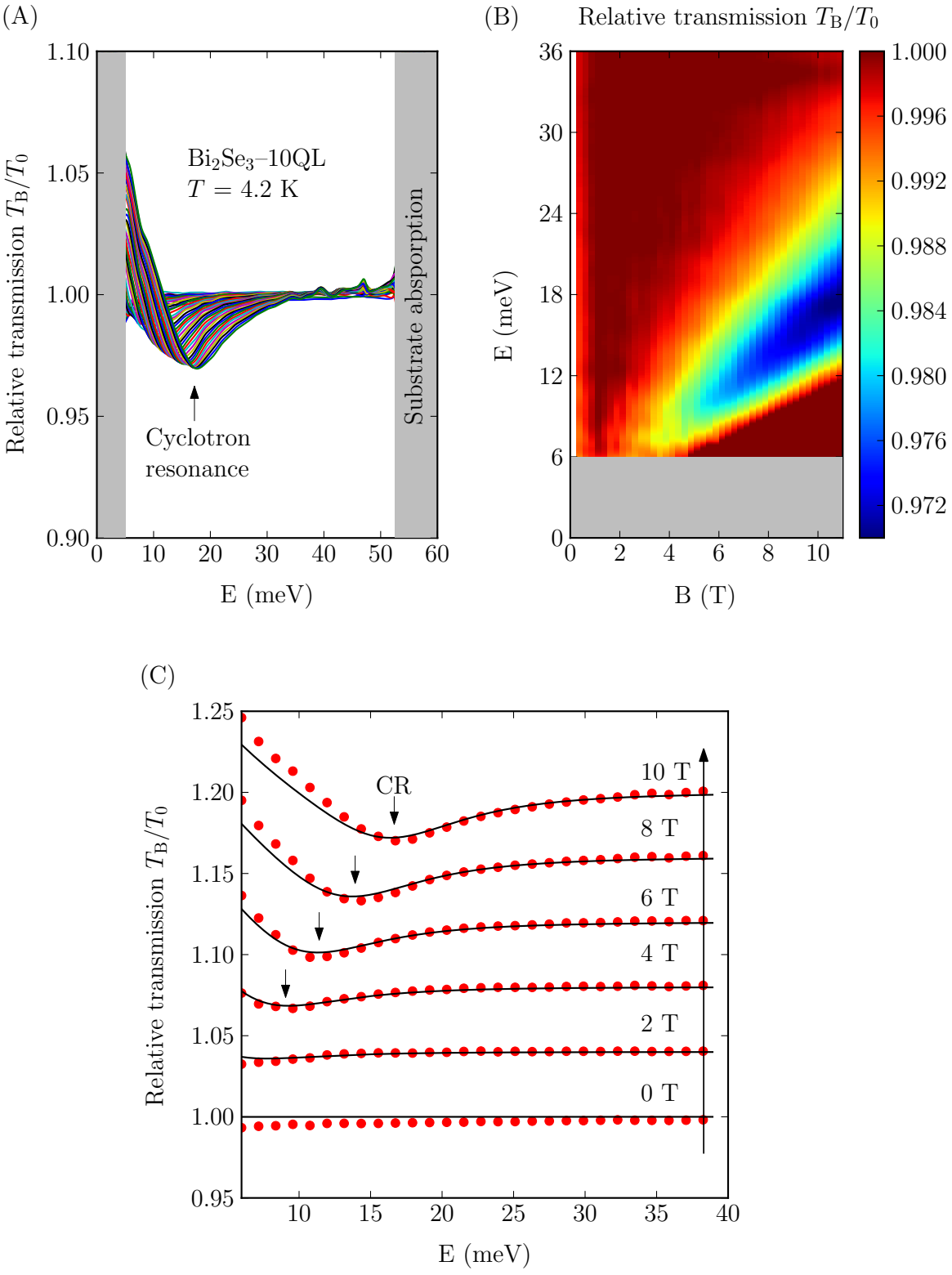

Fig. 5.3: Relative transmission of 10QL Bi_2Se_3 (A) represented also as a heatmap (B). The quasi-classical fit (lines) of the cyclotron resonance (marked by arrows) is depicted in (C) (the spectra are shifted by 0.04 for clarity).

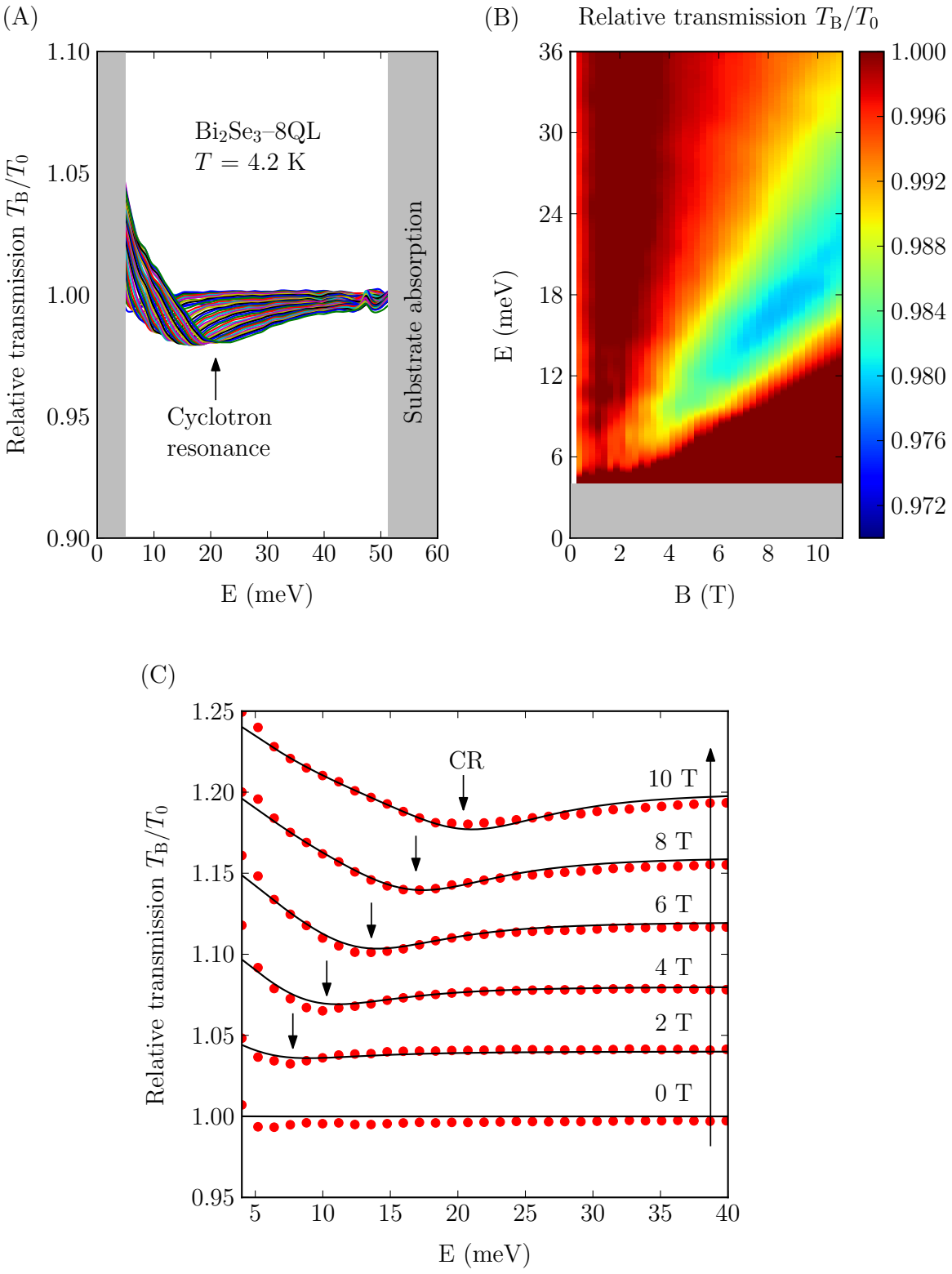

Fig. 5.4: Relative transmission of 16QL Bi_2Se_3 (A) represented also as a heatmap (B). The quasi-classical fit (lines) of the cyclotron resonance (marked by arrows) is depicted in (C) (the spectra are shifted by 0.04 for clarity).

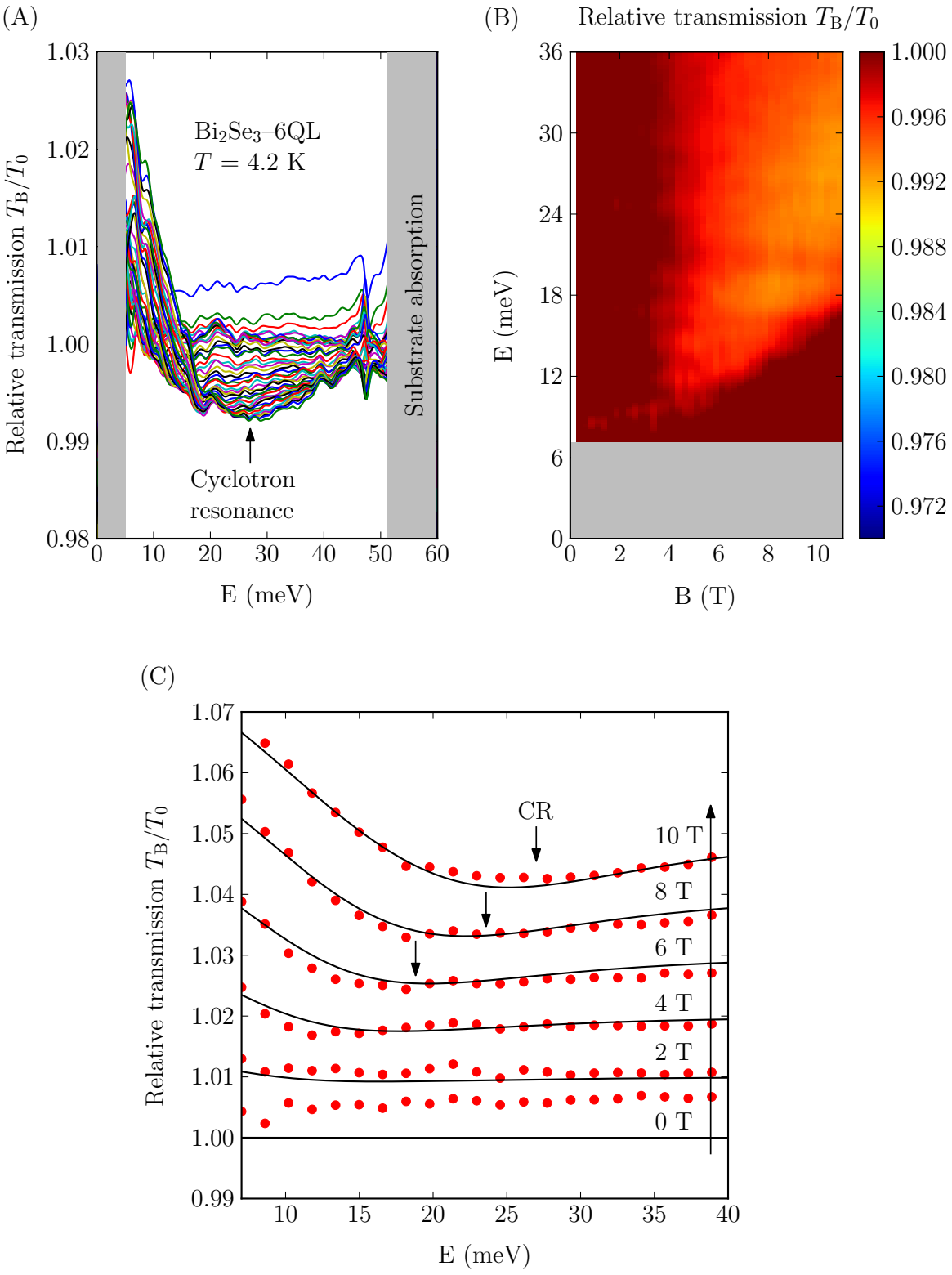

Fig. 5.5: Relative transmission of 6QL Bi_2Se_3 (A) represented also as a heatmap (B). The quasi-classical fit (lines) of the cyclotron resonance (marked by arrows) is depicted in (C) (the spectra are shifted by 0.01 for clarity).

As we can see from the CR spectra, the signal strength scales with the thickness of the Bi_2Se_3 layer. This spectral or Drude weight, approximately describing the strength of the CR absorption in the quasi-classical limit [55], is defined as $\mathcal{D} = 2e^2 E_F/4\hbar^2$. This formula has been deduced for graphene, with a twice higher degeneracy, but remains qualitatively valid also for other 2D gases of massless particles (such as on surfaces of topological insulators).

Thus, the thicker layers, with typically high carrier concentrations [27], give rise to bigger Drude weigth. On the other hand, higher concentration of charge carriers also require higher magnetic fields to achieve the corresponding quantum limit, with only the lowest Landau level occupied with electrons. This trade-off between the necessary strength of the magnetic field and the transmission signal, lead us to choose the 10QL sample for high-field experiments, in which the quantum limit is expected to be achieved around 30 T [54].

5.2 High-field magneto-transmission spectra

To fit the 10QL sample into the probe compatible with the 34mm-diameter bore of the high-field magnet, its size had to be reduced down to smaller dimensions. Nevertheless, we assume that the sample was homogeneous and it does not matter what part of the sample was cut.

The figure 5.6 shows relative magneto-transmission spectra in the fields up to 30 T. To our surprise, no indication of classical-to-quantum transition has been observed in the response. The cyclotron resonance remained single mode and retained nearly perfect linear in B dependence. This is in contrast with expectations for a Dirac-type system reaching its quantum limit, which is characterized by linear in $\sqrt{B}$ dependence of cyclotron resonance as described in 3.2.1.

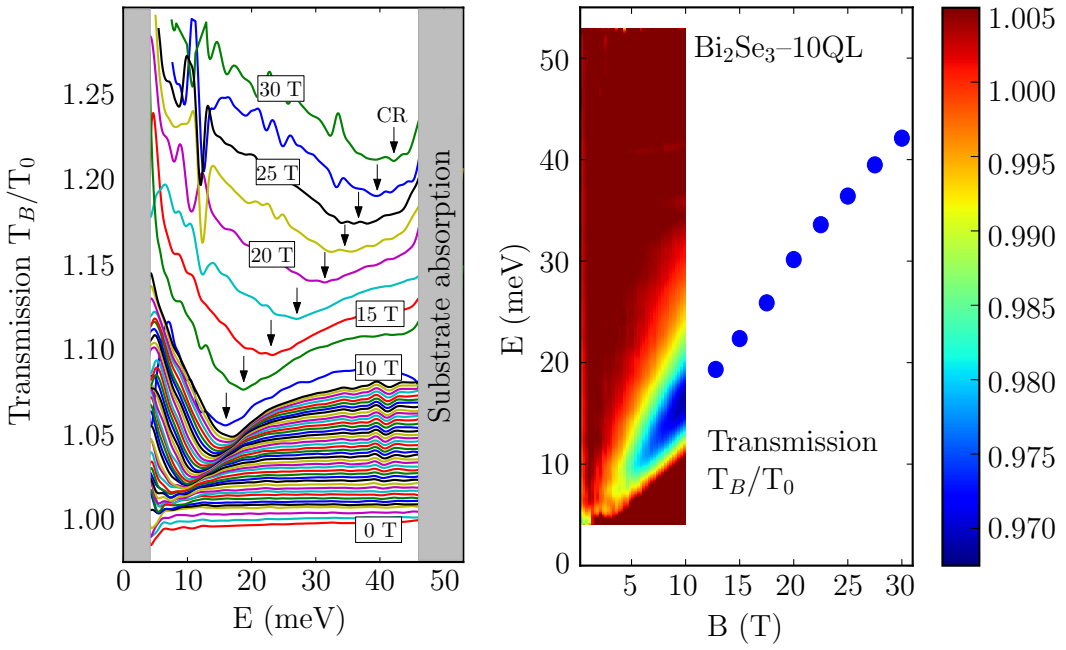

Fig. 5.6: Left: relative transmission spectra of 10QL Bi_2Se_3 with unexpected linear in B dependence of cyclotron resonance (marked by arrows). Right: heatmap plot of relative transmission in low fields and positions of CR in high fields.

This unexpected and very simple behaviour in high magnetic fields is not in line with findings of other experimental techniques, such as Faraday rotation [54] and magneto-transport [27]. At present, we do not see any straightforward explanation, which would provide us with a united picture comprising results of all performed experiments. As for the high-field infrared magneto-optics, the observed response may be described in terms of an ordinary gas of massive particles.

5.3 Magneto-transport measurement

Transport measurements in the van der Pauw configuration were realized as a supplementary method to determine approximate carrier concentration. Two of the smaller pieces of 10QL Bi_2Se_3 were attached to transport sample holder and four silver wires were glued to the corners of the sample using silver paste. Whole set was inserted into the probe and evacuated in the same manner as in the optical experiments. The measurements were performed also at LNCMI in the liquid helium cooled magnet at fields up to 16 T at temperatures at 1.4 K with the help of Dr. Benjamin Piot, responsible for magneto-transport experiments at LNCMI.

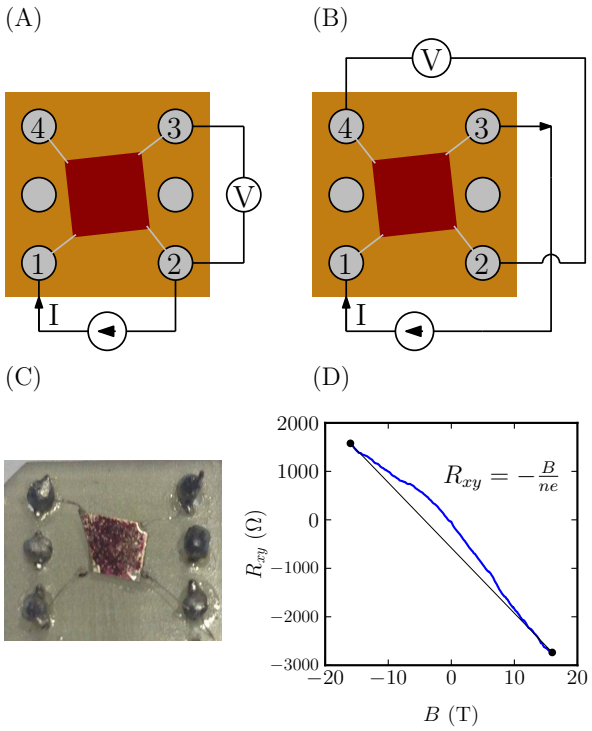

Fig. 5.7: (A) one of the configuration for measuring the resistivity of a sample. (B) one of the configurations for measuring the Hall coefficient. (C) the picture of the sample with the silver wires soldered to the pins. (D) data from Hall measurements (blue) and linear fit (black).

Let us now briefly review the standard van der Pauw method allowing us to explore transport properties of samples with approximately rectangular shapes. First we needed to obtain sheet resistance of the samples, using van der Pauw formula

$$\exp(-\pi R_{34}/R_s) + \exp(-\pi R_{41}/R_s) = 1, \tag{5.1}$$

where R_{34} is resistance between the points 3 and 4, R_{41} is resistance between the points 4 and 1 and R_s is the sheet resistance. From the Drude model the conductivity reads

$$\sigma = 1/\rho = 1/R_s = ne\mu, \tag{5.2}$$

and Hall coefficient $R_{\mathrm{H}} = B/ne$ for 2D materials. Hall coefficient can be extracted from the linear slope of the the field dependent transverse resistivity.

Obtained values for carrier densities are $5.23 \times 10^{16}\,\mathrm{cm}^{-2}$ and $4.7 \times 10^{16}\,\mathrm{cm}^{-2}$, which is much higher (4 orders of magnitude) than values obtained by Seongshik Oh *et. al* [27]. The reason is not exactly clear, however, as it could be the degradation of sample or incorrect contacting of the sample.

6 SUMMARY

Fabrication of samples with a sufficient quality, i.e., insulating in bulk but with well-defined Dirac-type surface states, is one of the major issues in the whole field of topological insulators. In particular, this issue is relevant for Bi_2Se_3, which is probably the most representative 3D topological insulator. Achieving this goal, the physics of topological matter could progress towards fascinating and still fairly exotic subjects such as hybrid structures between topological insulators and superconductors [4], detecting the Majorana fermions [6] or images of magnetic monopoles [56].

In this work, we examined the electronic states of Bi_2Se_3 heterostructure—one of the proposed solutions to the high intrinsic doping—by using the tools of infrared magneto-spectroscopy. We performed several experiments in quasi-classical regime (up to 11 T) for each of the four samples with different thickness (6, 8, 10, 16 QL) of Bi_2Se_3 layer. The observed magneto-optical response was in a good agreement with the simplified quasi-classical model for cyclotron resonance absorption. Therefore all relevant parameters (electron cyclotron mass, DC conductivity, line broadening and Drude optical weight) could have been extracted for each sample.

The intricate nature of such electronic system became apparent, when we performed the measurements in high magnetic fields (up to 30 T). On the selected sample, the cyclotron resonance response has been explored in magnetic fields, expected to be high enough to drive the system into quantum regime (with well-resolved Landau levels) and even into the corresponding quantum limit (with only the lowest level occupied). Instead of multi-mode $\sqrt{B}$-scaled cyclotron resonance absorption, typical of Dirac-type particles in the quantum regime, a conventional single-mode linear in B cyclotron resonance response has been observed.

At present, the interpretation of our observation is not straightforward. Our data are not in agreement with results and resulting expectations coming from other experimental techniques, namely low-field Faraday rotation [54] and high-field magneto-transport [27], which are consistent with Dirac-type character of studied charge carriers. In our case, the data may be explained using a model implying conventional massive particles.

Nevertheless, bismuth selenide and related heterostructures still belong to the perspective materials, utilizing the robust electron structure. So far, however, some the complications resulting from imperfect building blocks are yet to be overcome.

BIBLIOGRAPHY

[1] Ashcroft, N.; Mermin, N.: *Solid state physics*. Science: Physics, Saunders College, 1976, ISBN 9780030493461.

[2] Bernevig, B.; Hughes, T.: *Topological Insulators and Topological Superconductors*. Princeton University Press, 2013, ISBN 9780691151755.

[3] Klitzing, K. V.; Dorda, G.; Pepper, M.: New method for high-accuracy determination of the fine-structure constant based on quantized hall resistance. *Physical Review Letters*, vol. 45, no. 6, 1980: p. 494–497, doi:10.1103/PhysRevLett.45.494.

[4] Qi, X.; Zhang, S.: The quantum spin Hall effect and topological insulators. *Physics Today*, vol. 63, no. 1, 2010: p. 33, doi:10.1063/1.3293411.

[5] Zhang, H.; Liu, C.-X.; Qi, X.-L.; et al.: Topological insulators in Bi2Se3, Bi2Te3 and Sb2Te3 with a single Dirac cone on the surface. *Nature Physics*, vol. 5, no. 6, 2009: p. 438–442, doi:10.1038/nphys1270.

[6] Hasan, M. Z.; Kane, C. L.: Colloquium: Topological insulators. *Reviews of Modern Physics*, vol. 82, no. 4, 2010: p. 3045–3067, doi:10.1103/RevModPhys.82.3045.

[7] Avron, J. E.; Osadchy, D.; Seiler, R.: A topological look at the Quantum Hall effect. *Physics Today*, vol. 56, no. 8, 2003: p. 38–42, doi:10.1063/1.1611351.

[8] Qi, X. L.; Zhang, S. C.: Topological insulators and superconductors. *Reviews of Modern Physics*, vol. 83, no. 4, 2011, doi:10.1103/RevModPhys.83.1057.

[9] König, M.; Wiedmann, S.; Brüne, C.; et al.: Quantum spin hall insulator state in HgTe quantum wells. *Science (New York, N.Y.)*, vol. 318, no. 5851, 2007: p. 766–770, doi:10.1126/science.1148047.

[10] Kane, C. L.; Mele, E. J.: Z2 topological order and the quantum spin hall effect. *Physical Review Letters*, vol. 95, no. 14, 2005: p. 3–6, doi:10.1103/PhysRevLett.95.146802.

[11] Bernevig, B. A.; Hughes, T. L.; Zhang, S.-C.: Quantum Spin Hall Effect and Topological Phase Transition in HgTe Quantum Wells. *Science*, vol. 314, no. 5806, dec 2006: p. 1757–1761, doi:10.1126/science.1133734.

[12] Novoselov, K. K. S.; a.K. Geim, A. K.; Morozov, S. S. V.; et al.: Electric field effect in atomically thin carbon films. *Science*, vol. 306, 2004: p. 666–669, doi:10.1126/science.1102896.

[13] Castro Neto, a. H.; Guinea, F.; Peres, N. M. R.; et al.: The electronic properties of graphene. *Reviews of Modern Physics*, vol. 81, no. 1, 2009: p. 109–162, doi: 10.1103/RevModPhys.81.109.

[14] Moore, J. E.: The birth of topological insulators. *Nature*, vol. 464, no. 7286, 2010: p. 194–8, doi:10.1038/nature08916.

[15] Murakami, S.: Quantum spin hall effect and enhanced magnetic response by spin-orbit coupling. *Physical Review Letters*, vol. 97, no. 23, 2006: p. 1–4, doi: 10.1103/PhysRevLett.97.236805.

[16] Karalic, M.; Mueller, S.; Mittag, C.; et al.: Experimental signatures of the inverted phase in InAs/GaSb coupled quantum wells. *Physical Review B*, vol. 94, no. 24, 2016: p. 241402, doi:10.1103/PhysRevB.94.241402.

[17] Bernevig, B. A.; Zhang, S.-c.; Wu, C.: Quantum Spin Hall Effect. *Physical Review Letters*, vol. 96, no. 10, 2006: p. 1–4, doi:10.1103/PhysRevLett.96.106401.

[18] Fu, L.; Kane, C. L.: Topological insulators with inversion symmetry. *Physical Review B - Condensed Matter and Materials Physics*, vol. 76, no. 4, 2007: p. 1–17, doi:10.1103/PhysRevB.76.045302.

[19] Moore, J. E.; Balents, L.: Topological invariants of time-reversal-invariant band structures. *Physical Review B - Condensed Matter and Materials Physics*, vol. 75, no. 12, 2007: p. 3–6, doi:10.1103/PhysRevB.75.121306.

[20] Roy, R.: Z-classification of quantum spin Hall systems: An approach using time-reversal invariance. *Physical Review B*, vol. 79, no. 19, 2009: p. 195321, doi:10.1103/PhysRevB.79.195321.

[21] Hsieh, D.; Qian, D.; Wray, L.; et al.: A topological Dirac insulator in a quantum spin Hall phase. *Nature*, vol. 452, no. 7190, 2008: p. 970–974, doi:10.1038/nature06843.

[22] Xia, Y.; Qian, D.; Hsieh, D.; et al.: Observation of a large-gap topological-insulator class with a single Dirac cone on the surface. *Nature Physics*, vol. 5, no. 6, 2009: p. 18, doi:10.1038/nphys1274.

[23] Chen, Y. L.; Analytis, J. G.; Chu, J.-H.; et al.: Large Gap Topological Insulator Bi2Te3 with a Single Dirac Cone on the Surface. *Science*, vol. 325, no. 5937, 2009: p. 1–5.

[24] Hsieh, D.; Xia, Y.; Wray, L.; et al.: Observation of unconventional quantum spin textures in topological insulators. *Science (New York, N.Y.)*, vol. 323, no. 5916, 2009: p. 919–22, doi:10.1126/science.1167733.

[25] Mishra, S.; Satpathy, S.; Jepsen, O.: Electronic structure and thermoelectric properties of bismuth telluride and bismuth selenide. *Journal of Physics: Condensed Matter*, vol. 9, no. 2, 1997: p. 461–470.

[26] Hyde, G. R.; Beale, H. A.; Spain, I. L.; et al.: Electronic properties of Bi2Se3 crystals. *Journal of Physics and Chemistry of Solids*, vol. 35, no. 12, 1974: p. 1719–1728, doi:10.1016/S0022-3697(74)80186-1.

[27] Koirala, N.; Brahlek, M.; Salehi, M.; et al.: Record Surface State Mobility and Quantum Hall Effect in Topological Insulator Thin Films via Interface Engineering. *Nano Letters*, vol. 15, no. 12, 2015: p. 8245–8249, doi:10.1021/acs.nanolett.5b03770.

[28] Brahlek, M.; Koirala, N.; Salehi, M.; et al.: Emergence of decoupled surface transport channels in bulk insulating Bi2Se3 thin films. *Physical Review Letters*, vol. 113, no. 2, 2014: p. 1–5, doi:10.1103/PhysRevLett.113.026801.

[29] Checkelsky, J. G.; Hor, Y. S.; Cava, R. J.; et al.: Bulk band gap and surface state conduction observed in voltage-tuned crystals of the topological insulator Bi2Se3. *Physical Review Letters*, vol. 106, no. 19, 2011: p. 4–7, doi:10.1103/PhysRevLett.106.196801.

[30] Analytis, J. G.; Chu, J. H.; Chen, Y.; et al.: Bulk Fermi surface coexistence with Dirac surface state in Bi2 Se3: A comparison of photoemission and Shubnikov-de Haas measurements. *Physical Review B - Condensed Matter and Materials Physics*, vol. 81, no. 20, 2010: p. 1–5, doi:10.1103/PhysRevB.81.205407.

[31] Hor, Y. S.; Williams, A. J.; Checkelsky, J. G.; et al.: Superconductivity in CuxBi2Se3 and its implications for pairing in the undoped topological insulator. *Physical Review Letters*, vol. 104, no. 5, 2010: p. 3–6, doi:10.1103/PhysRevLett.104.057001.

[32] Vaško, A.; Tichý, L.; Horák, J.; et al.: Amphoteric nature of copper impurities in Bi2Se3 crystals. *Applied Physics*, vol. 5, no. 3, 1974: p. 217–221, doi:10.1007/BF00928132.

[33] Hsieh, D.; Xia, Y.; Qian, D.; et al.: A tunable topological insulator in the spin helical Dirac transport regime. *Nature*, vol. 460, no. 7259, 2009: p. 1101–5, doi:10.1038/nature08234.

[34] Ren, Z.; Taskin, A. A.; Sasaki, S.; et al.: Optimizing Bi2-xSbxTe3-ySey solid solutions to approach the intrinsic topological insulator regime. *Physical Review B - Condensed Matter and Materials Physics*, vol. 84, no. 16, 2011: p. 1–6, doi: 10.1103/PhysRevB.84.165311.

[35] Liu, M.; Chang, C. Z.; Zhang, Z.; et al.: Electron interaction-driven insulating ground state in Bi 2Se3 topological insulators in the two-dimensional limit. *Physical Review B - Condensed Matter and Materials Physics*, vol. 83, no. 16, 2011: p. 1–6, doi:10.1103/PhysRevB.83.165440.

[36] Chen, J.; Qin, H. J.; Yang, F.; et al.: Gate-voltage control of chemical potential and weak antilocalization in Bi2Se3. *Physical Review Letters*, vol. 105, no. 17, 2010: p. 1–4, doi:10.1103/PhysRevLett.105.176602.

[37] Guo, X.; Xu, Z. J.; Liu, H. C.; et al.: Single domain Bi2Se3 films grown on InP(111)A by molecular-beam epitaxy. *Applied Physics Letters*, vol. 102, no. 15, 2013: p. 2011–2015, doi:10.1063/1.4802797.

[38] Wang, Z. Y.; Guo, X.; Li, H. D.; et al.: Superlattices of Bi2Se3/In2Se3: Growth characteristics and structural properties. *Applied Physics Letters*, vol. 99, no. 2, 2011: p. 2011–2014, doi:10.1063/1.3610971.

[39] Brahlek, M.; Bansal, N.; Koirala, N.; et al.: Topological-metal to band-insulator transition in (Bi1-x Inx)2Se3 thin films. *Physical Review Letters*, vol. 109, no. 18, 2012: p. 1–5, doi:10.1103/PhysRevLett.109.186403.

[40] Bansal, N.; Kim, Y. S.; Brahlek, M.; et al.: Thickness-independent transport channels in topological insulator Bi2Se3 thin films. *Physical Review Letters*, vol. 109, no. 11, 2012: p. 1–5, doi:10.1103/PhysRevLett.109.116804.

[41] Emziane, M.; Marsillac, S.; Bern??de, J. C.: Preparation of highly oriented alpha-In2Se3 thin films by a simple technique. *Materials Chemistry and Physics*, vol. 62, no. 1, 2000: p. 84–87, doi:10.1016/S0254-0584(99)00145-5.

[42] Orlita, M.; Escoffier, W.; Plochocka, P.; et al.: Graphene in high magnetic fields. *Comptes Rendus Physique*, vol. 14, no. 1, 2013: p. 78–93, doi:10.1016/j.crhy.2012.11.003.

[43] Mittendorff, M.; Orlita, M.; Potemski, M.; et al.: Intraband carrier dynamics in Landau-quantized multilayer epitaxial graphene. *New Journal of Physics*, vol. 16, no. 12, 2014: p. 123021, doi:10.1088/1367-2630/16/12/123021.

[44] Faugeras, C.; Berciaud, S.; Leszczynski, P.; et al.: Landau level spectroscopy of electron-electron interactions in graphene. *Physical Review Letters*, vol. 114, no. 12, 2015: p. 1–5, doi:10.1103/PhysRevLett.114.126804.

[45] Orlita, M.; Potemski, M.: Dirac electronic states in graphene systems: Optical spectroscopy studies. *Semiconductor Science and Technology*, vol. 25, no. 6, 2010: p. 063001, doi:10.1088/0268-1242/25/6/063001.

[46] Analytis, J. G.; McDonald, R. D.; Riggs, S. C.; et al.: Two-dimensional surface state in the quantum limit of a topological insulator. *Nature Phys.*, vol. 6, no. 12, 2010: p. 960, doi:10.1038/nphys1861.

[47] Ayala-Valenzuela, O. E.; Analytis, J. G.; Chu, J.-H.; et al.: The surface-state of the topological insulator Bi2Se3 revealed by cyclotron resonance. *Advanced Materials*, vol. arxiv:1004, 2010: p. 2–5.

[48] Sadowski, M. L.; Martinez, G.; Potemski, M.; et al.: Magneto-Spectroscopy of Epitaxial Graphene. *International Journal of Modern Physics B*, vol. 21, no. 08n09, 2007: p. 1145–1154, doi:10.1142/S0217979207042586.

[49] Witowski, a. M.; Orlita, M.; Stepniewski, R.; et al.: Quasi-classical cyclotron resonance of Dirac fermions in highly doped graphene. *Physical Review B*, vol. 82, no. 16, 2010: p. 6, doi:10.1103/PhysRevB.82.165305.

[50] BRUKER OPTIK GbmH, IFS 66v/S User's manual. Available from docplayer.net/22047070-Ifs-66v-s-user-s-manual.html, Accessed 23/04/2017.

[51] Griffiths, P.; De Haseth, J.; Winefordner, J.: *Fourier Transform Infrared Spectrometry*. Chemical Analysis: A Series of Monographs on Analytical Chemistry and Its Applications, Wiley, 2007, ISBN 9780470106297.

[52] Rogalski, A.: Infrared detectors: An overview. *Infrared Physics and Technology*, vol. 43, no. 3-5, 2002: p. 187–210, doi:10.1016/S1350-4495(02)00140-8.

[53] The magnets. Available from http://lncmi-g.grenoble.cnrs.fr/spip.php?rubrique110&lang=en, Accessed 23/04/2017.

[54] Wu, L.; Salehi, M.; Koirala, N.; et al.: Quantized Faraday and Kerr rotation and axion electrodynamics of a 3D topological insulator. *Science*, vol. 354, no. 6316, 2016: p. 1124–1127, doi:10.1126/science.aaf5541.

[55] Orlita, M.; Crassee, I.; Faugeras, C.; et al.: Classical to quantum crossover of the cyclotron resonance in graphene: A study of the strength of intraband

absorption. *New Journal of Physics*, vol. 14, 2012, doi:10.1088/1367-2630/14/9/095008.

[56] Bansil, A.; Lin, H.; Das, T.: Colloquium: Topological band theory. *Reviews of Modern Physics*, vol. 88, no. 2, 2016: p. 1–37, doi:10.1103/RevModPhys.88.021004.